This is an Accepted Manuscript of an article published by Taylor & Francis in Journal of Sustainable Cement Based Materials on Oct 7, 2025, available at: https://doi.org/10.1080/21650373.2025.2565293

CO₂-injected Cement Paste: Insights into Microstructural and Chemo-mechanical Changes

Yogiraj Sargam¹, Sean Monkman², Vishnu Chaudhari³

Abstract

The microstructural and chemo-mechanical phase characterization of cement paste injected with CO_2 was performed in this study using analytical techniques such as nanoindentation, SEM-EDS, and ICP-OES. Quantitative evidence of the formation of carbonates through CO_2 mineralization was obtained, with CO_2 -injected pastes showing 0.5-1.5% (by volume) higher carbonates than control pastes (within the expected range based on the dosage). The carbonates precipitated mostly around the cement grains and appeared in locations also corresponding with high density and lower Ca/Si C-S-H, forming a reinforced product with relatively higher indentation modulus. This improvement in nanomechanical property also fostered corresponding improvements in the macromechanical properties such as bulk modulus and compressive strength. The findings from this study improve the overall understanding of the CO_2 -injected cementitious systems and can potentially assist their widespread adoption.

Keywords: Portland Cement; CO₂ Utilization; Nanoindentation; SEM-EDS

¹ **Corresponding author**; <u>yogirajsargam@gmail.com</u>; CarbonCure Technologies, 161 Joseph Zatzman Drive, Dartmouth B3B 1M7, Canada

² sean.monkman@gmail.com; Six Down Consulting, Austin, Texas, USA

³ <u>vchaudhari@carboncure.com</u>; CarbonCure Technologies, 161 Joseph Zatzman Drive, Dartmouth B3B 1M7, Canada

1. Introduction

CO₂ utilization in concrete involves the beneficial use of CO₂ in the production of concrete products or in the treatment of concrete wastes. Compared to utilization approaches to make chemicals and synthetic fuels, the concrete industry offers mineralization of CO₂ that demonstrates both scalable and permanent carbon removal [1]. Further, the opportunity for CO₂ utilization, for both carbon impact and commercialization, is greatest within the built environment [2].

The CO₂ has been employed as an admixture in ready mixed concrete production [3]. It reacts with calcium from the cement to form CaCO₃ and influence the cement hydration. According to Berger et al. [4], CO₂ reacts with hydrating cement in the presence of water to form calcium carbonate and C-S-H gel (the example of tricalcium silicate is related in Eq. 1).

$$3\text{CaO}\cdot\text{SiO}_2 + (3-x)\text{CO}_2 + y\text{H}_2\text{O} \rightarrow x\text{CaO}\cdot\text{SiO}_3\cdot y\text{H}_2\text{O} + (3-x)\text{CaCO}_3$$
 (1)

The CO₂ is permanently converted into a mineral, and the mineralization can improve the compressive strength of concrete, as shown in Fig. 1. The figure plots the 28-day compressive strength of seven different concrete mixes obtained from various ready-mix concrete producers employing a CO₂ utilization technology where carbon dioxide is added as an admixture. A complete dataset with mix designs is provided in section 1 of the Supplementary Information. Across a range of water-to-cementitious (w/cm) and binder compositions, CO₂ can be observed to increase the strength of concrete by 5 to 20%, which can be leveraged to optimize mixes with reduced cement contents.

Several studies in the literature have examined the use of CO_2 as an admixture in concrete, focusing on its effects on fresh properties and rheology [5,6], compressive strength [3,7], durability [7,8], and, in some cases, environmental impact [9,10]. Many studies [11–14] are also focused on investigating the underlying mechanism of CO_2 utilization as an admixture. For example, Zajac et al. [11] studied the carbonation mechanism of Portland clinker in a

custom-designed wet reactor under a constant flow of CO₂. Their findings revealed that clinker carbonation is a complex, multistage dissolution—precipitation process, where different phases dissolve at different times and the composition of the precipitates evolves over the course of the reaction. The primary carbonation products were identified as calcium carbonate (with calcite as the dominant polymorph) and amorphous alumina-silica gel. Although these results were not obtained in the context of CO₂ injection in fresh concrete, the reaction pathways and rate-limiting factors observed share important similarities with those expected during CO₂ injection in fresh concrete.

How the CO₂ can be added to concrete as an admixture and improve the compressive strength of concrete has heretofore been not explained. The specific reasons for this improvement are the subject of the present inquiry. A previous study [13] on the model C₃S system showed that CO₂ injection led to the precipitation of both C-S-H fibrils and CaCO₃ particulates, though their impact on mechanical properties or contribution to the strength improvement was undetermined. Another study [14] proposed the mechanism of hydration effects of CO₂ mineralization in the cement system, indicating the concentration of calcium ions in the pore solution as the driving force for CO₂ mineralization reaction and its associated chemical and physical effects. Considering the stoichiometry of the reactants and products, Monkman et al [5] proposed a schematic of the simultaneous hydration and CO₂ mineralization reactions. It was shown that as CO₂ is injected shortly after hydration starts, it leads to the formation of CaCO₃, H₂O, C-S-H gel with lower Ca/Si (1.2), and 30-40% less Ca(OH)₂ compared to the baseline condition of no CO₂ injection. In addition, it was also demonstrated that while just the hydration pathway results in 11% decrease in volume, the combined CO₂ injection and hydration results in a 19% increase in volume over its starting conditions. This study further analyzed the effect of CO₂ mineralization on the rheological properties of self-consolidating concrete but not on the mechanical properties. A recent research [15] has used Raman microscopy and indentation approaches to investigate

bicarbonate-substituted alite as a model system for understanding the underlying chemomechanics of cement carbonation, where the formation of a CaCO₃/C-S-H composite phase was observed. However, this study did not provide direct evidence of composite leading to improvements in mechanical performance. Furthermore, given that the investigation was done on a model alite system with bicarbonate substitution, it is uncertain whether the mechanism will be the same in a more complicated cementitious system with CO₂ injection.

In summary, the mechanism underlying the strength improvement due to CO₂ mineralization, including the mechanical and microstructural changes, is not yet fully explained and understood, indicating the need for further research in this field. To address this gap, the objective of this study was to analyze the microstructural and chemo-mechanical phase changes occurring in a CO₂-injected cement paste at various ages. The analysis focused on the micro and nanoscale levels of the cement paste and was performed using characterization techniques such as nanoindentation, Scanning Electron Microscopy with Energy-dispersive spectroscopy (SEM-EDS), and Inductively coupled Plasma with Optical emission spectroscopy (ICP-OES). Additionally, the determined characteristics were correlated with the macro-scale mechanical properties such as compressive strength and homogenized elastic modulus. The novelty of this work lies in its integrated multi-scale approach that directly links CO₂-induced microstructural transformations with measurable improvements in mechanical performance in real cementitious systems. Unlike prior studies conducted on model compounds or with limited characterization, this study provides direct mechanistic evidence of how CO₂ mineralization reinforces C-S-H and densifies the paste matrix, thereby offering new insights into the fundamental role of CO₂ in enhancing concrete performance and advancing its sustainable utilization.

2. Materials and Methods

2.1 Materials

The materials used in this study were Portland cement, water and CO₂. The manufacturer-provided properties of cement (ASTM C150 [16] Type I/II) are shown in Table 1. The CO₂ gas used was commercial grade (99.9% purity) and was supplied by BOC gases.

2.2 Sample preparation

Cement paste samples, at a water-binder ratio of 0.5 (800 g of cement and 400 g of water), were prepared for the characterization experiments in this study. CO₂ was employed as an admixture at a dose of 0.3% by weight of cement (dose selected based on previous study [17]). The mixing procedure comprised the following steps: add the required quantity of cement to water in a paste blender, mix at 4000 rpm for 60 seconds, mix at 12000 rpm for 30 seconds, pause for 15 seconds, mix for 30 seconds at 12000 rpm while, if appropriate, injecting the required amount of gaseous CO₂ as controlled by a mass flow meter. A portion of the paste obtained thereafter was immediately placed in an isothermal calorimeter for the heat of hydration measurements. From the fresh paste, specimens were sampled at 5 minutes for SEM observation, and the hydration was stopped using isopropanol. Some of the fresh paste was used to extract pore solution until 6 hours of hydration (detailed later in this section). The remainder of the paste was then cast in 50 mm (2-inch) cubes for subsequent tests including compressive strength, nanoindentation, and SEM-EDS. Cylindrical samples of 50 mm x 100 mm (2-in. x 4-in.) were also cast for pore solution extraction at later ages (24 hours, 17 day, and 28 day). The cast specimens were demolded after 24 hours and subsequently cured in limewater-curing baths (ASTM C192 [18]) until the testing ages of 7 and 28 days. At the required testing age, the hydration was arrested through a solvent exchange method using isopropanol.

Compressive strength testing was performed on cube samples, following ASTM C109 [19], with three specimens tested at each age. The specimen preparation for nanoindentation and SEM-EDS analyses involved cutting the 50 mm cubes down to 25 mm cubes, drying overnight at 40° C, and impregnating them in epoxy for 12 hours under vacuum. The 5-minute specimens were obtained in powder form after the solvent exchange and were directly impregnated in epoxy. After epoxy-impregnation, all specimens were polished using silicon carbide papers gradually from 180 grit (80 µm) on through 240, 320, 400, 600, 800 to 1200 grit (5 µm), spending around 15 seconds at each stage. Two further polishing steps were completed using diamond slurry: 3-µm for 60 seconds and finally down to 1-µm for 30 seconds. To make the polished specimens conductive, they were sputter-coated with a 2 nm thick layer of iridium before microscopic analysis.

This work also involved characterization of pore solution through ICP-OES measurements for samples aged 5 minutes, 1, 2, 4, 6, and 24 hours, and 7 and 28 days. For samples up to 6 hours old, a syringe filter and cotton balls were used in conjunction with a pore press [20] to extract the pore solution. Specifically, two cotton balls weighing approximately 1.20g were compressed into the base of a 60mL plastic syringe with a 0.2-µm filter attached to the outlet. The syringe was then filled with cement paste and placed into the pore press connected to an air compressor to extract approximately 10mL of solution into a small beaker. Samples aged 24 hours, 7 days, and 28 days used 50 mm x 100 mm (2-in. x 4-in.) cylindrical samples subjected to pressures up to 200 bar as applied for 2 to 3 minutes to obtain the required amount of pore solution. The extracted pore solution from both early and later age samples was subsequently acidified using nitric acid before undergoing ICP-OES analysis.

2.3 Test methods

2.3.1 Isothermal calorimetry

Isothermal heat conduction calorimetry was performed with a Calmetrix iCal 8000 calorimeter. 50-gram samples of paste were placed in the calorimeter within 60

seconds of the conclusion of the mixing, with calorimeter equilibrated to 20 °C and the data was collected for 24 hours. The rate of heat generation was measured and normalized to the sample's cement content. The measured rate of heat was also used to calculate the cumulative heat and is presented as the energy.

2.3.2 SEM-EDS

Scanning Electron Microscopy (SEM) was performed with an FEI Quanta-FEG 250 in backscatter electron (BSE) mode. The energy-dispersive spectroscopy (EDS) system was equipped with Oxford instruments' X-Max 80 SDD detector. The microscope was operated at accelerating voltage and a working distance of 10kV and 10 mm, respectively, based on the Monte Carlo simulations performed in a previous work [21]. The specimens were imaged to obtain micrographs at increasing magnifications of 10X to 1500X. The quantitative analysis, however, was performed on the micrographs of the same magnification. EDS elemental mapping was done at 500X magnification. High-quality spectra were acquired at an x-ray count rate of 15 to 20k counts per second with 30% dead time at process time 4. The elemental maps of C, O, Na, Mg, Al, Si, S, K, and Ca were collected at 100 µs per pixel.

2.3.3 Nanoindentation

After SEM-EDS analysis, nanoindentation was performed on polished paste specimens using a Hysitron TI 950 Tribolndenter equipped with a Berkovich probe. Force-controlled (3 mN) indentations were carried out in a trapezoidal loading pattern. It involved loading at a rate of 10 nm/s for 20 seconds, holding for 2 seconds, and unloading for 20 seconds. The average maximum indentation depth (h_{max}) varied with the sample age but was in the range of 200-500 nm. Indents were done in a 20 × 10 grid with an even spacing of 10 µm, obtaining 200 indents per specimen, considered statistically representative for cement pastes [22,23]. The load-displacement curves were obtained for every indent

from which the indentation hardness (H) and indentation modulus (M) were calculated as per the Eqs. (2-3) [24].

$$H = \frac{P_{max}}{A_c} \tag{2}$$

$$M = \frac{\sqrt{\pi}}{2\beta} \frac{S}{\sqrt{A_c}} \tag{3}$$

where P_{max} is the maximum applied force (3 mN in this study), A_c is the projected area of contact calculated using the Oliver and Pharr method [25], S is the unloading indentation stiffness, and $\beta = 1.034$ for the Berkovich indenter.

2.3.4 ICP-OES

The extracted pore solution was analyzed for its elemental concentration using inductively coupled plasma optical emission spectroscopy (ICP-OES). To stabilize the solution and prevent precipitation, samples were diluted with 2% HNO₃ at a dilution factor of 5.5. Liquid argon (99.99% purity) was used for plasma generation, nebulization, and as auxiliary gas. For K and Na spectral lines, the plasma viewing was fixed as radial, while for all other elements, it was axial. Before measuring the concentration of actual samples, calibration was performed for each element using standard solutions. The composition of the standard solution was adjusted to cover the entire range of concentrations measured in this study. Hence, the actual values of elemental concentrations were obtained by interpolation. The obtained values were also corrected using the dilution factor.

2.4 Homogenized elastic modulus

The nanomechanical properties obtained using nanoindentation were used to estimate the homogenized elastic modulus of the cement paste system. A homogenization approach based on the analytical Mori-Tanaka scheme [26] was used for this purpose, as successfully used by many researchers [27–29]. The scheme defines a composite as a reference matrix reinforced by spherical

inclusions and uses a homogenized bulk (k_{hom}) and shear modulus (τ_{hom}) to calculate the homogenized elastic modulus (E_{hom}) as follows [27]:

$$k_{hom} = \frac{\sum_{i}^{V} k_{i} \left(1 + A_{r} \left(\frac{k_{i}}{k_{r}} - 1 \right) \right)^{-1}}{\sum_{i}^{V} k_{i} \left(1 + A_{r} \left(\frac{k_{i}}{k_{r}} - 1 \right) \right)^{-1}}$$
(4)

$$\tau_{hom} = \frac{\sum_{i} V_{i} \tau_{i} \left(1 + B_{r} \left(\frac{\tau_{i}}{\tau_{r}} - 1 \right) \right)^{-1}}{\sum_{i} V_{i} \left(1 + B_{r} \left(\frac{\tau_{i}}{\tau_{r}} - 1 \right) \right)^{-1}}$$

$$(5)$$

$$E_{hom} = \frac{9k_{hom}\tau_{hom}}{3k_{hom} + \tau_{hom}} \tag{6}$$

$$A_r = \frac{3k_r}{3k_r + 4\tau_r} \tag{7}$$

$$B_r = \frac{6k_r + 12\tau_r}{15k_r + 20\tau_r} \tag{8}$$

Where k_r and k_i are the bulk moduli of the reference medium and inclusion phases, respectively, and τ_r and τ_i are the respective shear moduli. The volume fraction of each inclusion phase is denoted by V_i . The bulk (k) and shear (τ) moduli of the reference medium (r) and each inclusion phase (i) are calculated by:

$$k_{r,i} = \frac{E_{r,i}}{3(1 - 2v_{r,i})} \tag{9}$$

$$\tau_{r,i} = \frac{E_{r,i}}{2(1+v_{r,i})} \tag{10}$$

Where E is the indentation modulus for each phase and v is the Poisson's ratio.

3. Results and Discussion

3.1 Heat of hydration and Compressive strength

The hydration kinetics of cement pastes were tracked during the first 24 hours, as shown in Fig. 2. Quantitative analysis of the calorimetry data is summarized in Table 2. The calorimetric set time increased by 8 minutes, suggesting a minimal effect of CO_2 injection on the setting characteristics of cement. The heat flow following the induction period (in the range of 2 to 8 hours) and the slope of the acceleration curve, however, were consistently higher in the CO_2 injected paste. The peak rate of heat and the slope were higher by 15% and 45%, respectively than those in the control paste. This indicated a higher rate of silicate (primarily C_3S) dissolution upon CO_2 injection. The sulfate depletion peak appeared slightly earlier in CO_2 injected paste (around 13 hours) than in control (around 15 hours). In addition to its effects on hydration kinetics, CO_2 injected paste also showed consistently higher cumulative heat (energy) than the control paste and was 7% greater at 24 hours.

Fig. 3 shows the compressive strength of paste samples aged 1, 7, and 28 days. The compared 1-day strengths of the two pastes were within the margin of variability. CO₂-injected paste, however, showed slight improvements of about 7% and 5% at 7 and 28 days, respectively.

3.2 Microstructural characterization

The BSE micrographs of polished paste specimens aged 5 minutes, 1 day, 7 days, and 28 days were captured to analyze their microstructures. Figs. S1-S4 in section 2 of the supplementary information show the micrographs at magnifications of 150X, 500X, and 1500X. As the 5-minute specimens were powdered and embedded in epoxy, their micrographs contained significant dark regions which referred only to epoxy, while the dark spots/regions in the micrographs of hardened specimens (1, 7, and 28 days) referred to pores and voids (nanometer to micrometer-sized). The other regions with varying grey

levels corresponded to clinker and hydrate phases. Microcracks, resulting possibly due to shrinkage, were also visible in some micrographs at higher magnifications (e.g., 1500X). From the visual observation of 1 to 28-day micrographs, reducing fraction of dark regions and corresponding densification of microstructure with age was apparent, attributable to the continued dissolution of clinker phases and precipitation of hydrates. However, neither the microstructures of the control nor the CO₂-injected pastes were visually discernible in this mode, with the various hydrate phases unable to be differentiated from the micrographs. Even by adjusting the brightness and contrast of the BSE micrographs, their grey level histograms could be segmented into only two major peaks representing the unhydrated cement particles and hydrates. Therefore, EDS mapping was employed to further distinguish various phases.

The elemental mapping of the micrographs (500× magnification) was performed to obtain compositional (chemical) contrast in phases. An example of the elemental mapping (for the control at 7 days) is shown in Fig. S5 (supplementary information section 2). The maps were further used to identify various phases using the *AZtec NanoAnalysis* software. It involves grouping the pixels with similar spectral content based on the difference in intensity of various elements. The analysis has previously been used [21] satisfactorily, assigning around 95% of the pixels from a BSE micrograph with various clinker and hydrate phases.

The micrographs obtained from the phase analysis are presented in Fig. 4 with false colors attributed to various assigned phases. The blue-colored region corresponded to the main hydration products: CH and C-S-H. Morphologically, two types of C-S-H are generally observed in the hydrated cement paste: outer product (OP) and inner product (IP). From a physical property perspective also, two types have been proposed [30]: low density (LD) and high density (HD), with their average packing density being 0.64 and 0.75, respectively [22]. LD C-S-H preferentially forms in the capillary space, while the HD C-S-H forms in more

confined regions within the original boundaries of cement [22]. Microscopic evidence [31] suggesting similar formation regions of OP and IP led to the literature relating the OP to LD and IP to HD C-S-H and using them interchangeably. However, a recent study [32] states that the relation cannot be established straightforwardly since the former is directly observable while the latter is established from sorption experiments. Nevertheless, both are considered to correspond to similar geometries in the paste. Since the microscopic examination in this study was performed on polished specimens in backscatter mode (no morphological observations), and later nanoindentation results (section 3.4) were also related to the density of phases, the two C-S-H types are appropriately referred to here as LD and HD, instead of OP and IP. Right from the earliest examination time of 5 minutes (Fig. 4), shell formation (hydration products, shown in blue) occurred around most of the grains in both the control and CO₂ samples. Notably, the shells also formed around the limestone grains (shown in red) present in cement, consistent with TEM observations by Bazzoni [33] showing limestone surfaces acting as a substrate for nucleation of hydrates. The average EDS spectra of these shells showed prominent intensity peaks of calcium and silicon with the mean atomic Ca/Si ratios of 2.35 and 1.67 for the control and CO₂ samples, respectively. This pointed towards the shells being those of the main cement hydration product C-S-H. As Gallucci et al. [34] reported, the shells that form so early have their morphology, density, and orientation different from that of LD C-S-H. But the thin dense layer of the shell does consist of small C-S-H nuclei, and the layer can act as a substrate for the growth of LD C-S-H. The continued growth of C-S-H with age was apparent from the increasing area fraction of blue-colored regions in 1-day to 28-day micrographs (b to d and f to h in Fig. 4), although the effect of CO₂ injection on the bulk phase assemblage was not evident. However, the phase separation revealed the presence of calcium carbonate particles (shown in orange) in the 5-min, 1-day, and 7-day micrographs of CO₂-injected pastes. The particles were in trace quantities, with their volume fractions being around 1%,

1%, and 0.5%, respectively. This confirmed the occurrence of the CO_2 mineralization process resulting in precipitation of calcium carbonates, not observed in micrographs of the control paste. The lack of identified mineralized carbonate at 28 days is consistent with the hydration enhancing effect of finely divided limestone particles whereby these particles react with the aluminate phases to form hemi- and mono-carboaluminate [35].

An example of masked micrographs and their binary forms showing the mineralized carbonate particles are presented in Fig. 5. The mineralized CO₂ appeared to have precipitated mostly around the clinker and limestone grains, and the precipitates also appeared to be around precipitated C-S-H. The binary images were analyzed using ImageJ following the procedure outlined by Sargam et al. [21,36]. Fig. 5(c) shows the histogram of Feret diameter of mineralized carbonate products, including those formed at all three ages (5 min, 1 day, and 7 day). Out of around 200 products analyzed, around 75% were sized less than 5 μm, with the mean Feret diameter of 4.5 μm. It is worth mentioning that the individual products of in-situ mineralized calcium carbonate generally appear nanometer-sized [3,13,37], when observed in the secondary electron mode of a microscope at early age (a few hours of hydration). The micrometer size of products observed here in BSE mode can possibly be attributed to the coalescence of individual nanoscale products making them appear larger or precipitation of carbonates with C-S-H to form aggregated products of size larger than the individual products.

3.3 Chemical characterization

3.3.1 C-S-H composition

Extending the phase separation methodology allows for determining the chemical composition of LD and HD C-S-H. The composition of C-S-H is generally expressed by the atomic ratio of calcium to silicon (Ca/Si). The literature reports a wide range of Ca/Si, with most falling from 0.7 to 2.3 [38,39]. The average ratios determined in this study (Fig. 6) were in the range of 1.37 to 2.55. In

general, Ca/Si of LD and HD C-S-H increased from 1 to 7 days, after which the change was insignificant, consistent with the literature [39,40] reporting that C-S-H becomes compositionally more homogenous with age.

Concerning the effect of CO₂, mean Ca/Si of the C-S-H shell formed at 5 minute and HD C-S-H at 1 day (1.67 and 1.64, respectively) were lower in the case of CO₂-injected paste compared to those of control paste (2.35 and 2.15, respectively). The compositional differences in the C-S-H formed in the two pastes diminished at further analyzed ages of 7 and 28 days since most of the chemical activity due to CO₂ injection occurs within the first few minutes to hours. That CO₂ injection leading to a lower Ca/Si C-S-H can be attributed to the formation conditions of the C-S-H and is in general agreement with the stoichiometric changes in the hydration and CO₂ mineralization reactions. As shown in a recent study [5], the conventional hydration pathway proceeds through the reaction of 3CaO SiO₂ and 5.3H₂O forming 1.7CaO SiO₂ 4H₂O (C-S-H) and 1.3Ca(OH)₂. In the combined hydration and CO2 injection pathway, 3CaO SiO₂, 5H₂O and CO₂, H₂O react to form 1.2CaO SiO₂ 4H₂O (C-S-H), 0.8Ca(OH)₂, CaCO₃, and 1.2H₂O. This suggests that CO₂-injection leads to the formation of a reduced quantity of calcium hydroxide along with a C-S-H gel with a reduced Ca/Si. It is also noteworthy that CO₂-injection mostly affected the composition of HD C-S-H. As shown in Fig. 5, mineralized CO₂ forms calcium carbonate crystals on the surfaces of clinker grains, and the precipitation of HD C-S-H also occurs around these grains through an infilling or compaction of fragile early age inner product inside the shell [34]. This explains a significant effect of CO₂ mineralization only on the Ca/Si of shell and HD C-S-H and not on that of LD C-S-H.

3.3.2 Pore solution chemistry

The elemental molar concentrations of the extracted cement pore solutions were measured using ICP-OES and are shown in Fig. 7. The concentrations were measured at early ages (5 min, 1, 2, 4, 6, and 24 hours) as well as at later ages

(7 and 28 days). In general, the pore solution contained Ca, C, K, Na, and S in high concentrations, while the concentrations of Si, Al, Fe, and Mg were relatively low. A substantial drop in the Ca and S concentrations (around 65% and 70%, respectively) can be observed from 6 hour to 24 hour (1 day), mainly due to the depletion of sulfate in the formation of ettringite. From 1 day onwards, these concentrations remained relatively low, while significant increments in the C, Na, and K concentrations occurred. The increasing concentrations of alkalis (Na and K) can be attributed to their continuous release as clinker hydrates and the volume of the liquid phase present decreases [41].

At early age, the CO₂-injected samples contained relatively lower concentrations of Ca as compared to those in control samples. This can be attributed to the consumption of Ca²⁺ ions generated from the dissolution of clinker phases in the mineralization of CO₂. This early age effect, however, was reversed at later age, with Ca concentration being relatively higher in CO₂-injected samples' pore solution. Notably, the pore solution of CO₂-activated samples also contained higher concentrations of Na and K at later age, which indirectly pointed toward lower alkali uptake by the C-S-H formed in these samples. C-S-H has a layered structure with Ca-O layers sandwiched between silicate chains in a "dreierketten" arrangement, and the alkalis incorporate into the interlayer space and on the surface via a charge balance mechanism [42]. Based on the SEM evidence (sections 3.2 and 3.3.1) of mineralized CO₂ precipitating in the spaces of HD C-S-H, it can be hypothesized that CaCO₃ precipitates might have occupied the C-S-H interlayer spaces, thereby limiting the uptake of alkali ions. No significant effect of CO₂-injection on the pore solution concentrations of S was observed. Consistent with literature [43], the concentrations of Al, Si, and Mg were less than 1 mmol/l for both the control and CO₂-injected paste solutions. CO₂-injected solution, however, contained abnormally high concentrations of these elements at 28 days. The abnormality could either be attributed to the relatively lower reliability of low concentration elements measured using ICP-OES or to an increased alkali concentration of the CO₂-injected solution.

3.4 Mechanical characterization

3.4.1 Nanoindentation

The frequency distributions of indentation modulus (n = 200 indents per sample) are plotted in Fig. 8. Based on the literature [27,44,45], a bin size of 1 GPa was selected for plotting the distribution and for further deconvolution of the characteristic peaks. At all tested ages (1, 7, and 28 days), overlapping distributions of control and CO₂-injected samples can be observed. However, CO₂-injected samples exhibited higher peaks in the modulus range of around 20 to 40 GPa consistently at all ages. This range of modulus values corresponds to the C-S-H phase or its combination with other hydrates. Higher peaks in the case of CO₂-injected samples can possibly be attributed to the precipitation of C-S-H reinforced by calcium carbonate crystals formed from CO₂ mineralization. This became more evident from the deconvolution of peaks (Fig. 9) to identify mechanically distinct phases. A statistical Gaussian fitting method [27] was applied to the experimental probability density function (PDF) and to generate the theoretical PDF. The fitting of the corresponding cumulative density functions (CDFs) was also analyzed to obtain $R^2 > 0.9$ (fitted curves shown in Fig. S6 of the Supplementary information). The deconvolution resulted in four major phases (Fig. 10): LD C-S-H gel, HD C-S-H gel, CH/other hydrates, and clinker in the ascending order of indentation modulus. In the case of 1-day sample, fitting furnished an additional deconvoluted peak around 5 GPa, which referred to pores and/or defects. Due to a denser microstructure and lower porosity, this peak was not prominent at later ages. Investigating differences between the two conditions showed that CO₂-injection influenced the HD C-S-H, reinforcing the observation from SEM-EDS. In the case of CO₂ samples, the HD C-S-H curves were shifted slightly towards the right, suggesting higher mean indentation moduli imparted by CO₂ injection. This was consistently observed at all tested ages of 1, 7, and 28 days. The observed range of modulus values of

deconvoluted phases were closely aligned with some of the literature-reported values [46–50].

The increased modulus effect of CO₂-injection is shown in Fig. 10. The modulus of LD C-S-H was not significantly affected, with most of the values around 10 ± 2 GPa. A difference in the modulus of HD C-S-H was observed. At 1 day and 7 day, the moduli were 13.9 ± 0.4 and 14.6 ± 0.6 for the control and 15.6 ± 1.3 and 21.8 ± 3.3 GPa for the CO₂ samples, respectively. The corresponding mean values in the case of CO₂ samples were around 12% higher at 1 day and 50% higher at 7 days than those of the control samples. Due to relatively stable compositional homogeneity of C-S-H at later age [39,40], there was no notable difference in the modulus of control and CO₂ samples at 28 days. In addition, a higher mean modulus of CH/other hydrates was observed in the CO₂ samples; however, the difference was not statistically significant considering high standard deviations. The results presented above suggest that the mineralization of CO₂ may lead to the reinforcement of HD C-S-H with calcium carbonate crystals, thereby resulting in higher modulus and denser microstructure. Structurally, C-S-H itself is a nanocomposite with stacked lamellae formed by a double central layer of CaO octahedra inserted between two layers of SiO₄ tetrahedra [51]. The calcium carbonate particles precipitated due to in-situ mineralization of CO₂ are also nanometer-sized crystals [14,37]. Therefore, it can be hypothesized that the crystals of calcium carbonate reinforce the structure of HD C-S-H by either filling the interlayer gel pores or by simply filling the spaces between the HD C-S-H nanoparticles. Given that both the nano-entities (HD C-S-H and calcium carbonate) generally nucleate in confined spaces within the cement matrix, such as around the cement grains (Fig. 4), the reinforcement or interaction was highly probable. Besides, the reinforced product that formed showed modulus higher than that of HD C-S-H, similar to the observations by Chen et al. [22] concerning the identification of UHD (ultra-high density) C-S-H, a composite of HD C-S-H and CH that generally forms in low w/c systems, and exhibits mechanical properties intermediate between the two phases (HD C-S-H and CH).

The modulus of the reinforced product was also in agreement with the SEM-EDS observed changes in the chemical composition of C-S-H (section 3.3.1). The Ca/Si of HD C-S-H formed in CO_2 -injected paste was lower than that formed in control paste while the modulus was higher. This agrees with literature that suggests a C-S-H with a higher elastic moduli have a lower Ca/Si ratio [51,52]. It is generally agreed [52–54] that the modulus of C-S-H is dependent on the length of its silicate chain and packing density. Theoretically, where CO_2 mineralization impacts Ca (otherwise part of C-S-H as the double central layer of CaO octahedra) rather than Si (as part of layers of SiO_4 tetrahedra) an increase in the packing density seems to be the main reason behind the higher modulus of the reinforced product.

3.4.2 Homogenization

The phase moduli obtained from nanoindentation were upscaled to estimate the homogenized elastic moduli of the paste systems following the Mori-Tanaka scheme [Eqs. (4-10)]. The LD C-S-H was considered the reference matrix, while rest of the phases (HD C-S-H/calcite, CH/other hydrates, and clinker) were considered inclusions. The porosity was also considered an inclusion and was assessed by analyzing the SEM micrographs using the thresholding technique [55]. The total porosity of a cement paste system includes the pore volumes corresponding to the gel pores, capillary pores, and air voids. Since the interaction volume for nanoindentation is $\approx 0.6 \ \mu m^3$ [28], it is assumed that the pores smaller than this limit, mainly gel pores, would already be included in the nanoindentation results. Hence, only the volume of capillary pores and air voids were assessed from SEM micrographs of 150X and 10X magnifications, respectively. The total porosity thus obtained (Table 3) was accounted for to correct the volume fractions of the reference matrix and other phase inclusions. The indentation moduli and volume fractions of matrix and inclusion phases were then used to estimate the homogenized moduli of control and CO₂-injected pastes, as presented in Table 3.

In general, as the pastes aged, the porosity of both the pastes reduced and the homogenized moduli increased, attributable to the filling up of the matrix space due to continued hydration. CO₂-injected pastes showed higher homogenized modulus than control pastes. For example, the homogenized modulus of CO₂ paste at 7 day was around 35% higher than that of control paste. This also corresponded well with the higher indentation modulus of the HD C-S-H/calcite reinforced product formed in the case of CO₂-injected pastes and with the higher compressive strength (Fig. 3). The increased modulus and strength align well with the increase in volume of hydration products due to CO₂ injection [5]. As demonstrated by Monkman et al [5], while the hydration pathway results in an 11% decrease in volume of reaction products, the CO₂ injection pathway results in a 19% increase in volume over its starting condition, inferring that a CO₂ injected system contains 44% greater volume of hydration products than a control system. It can, therefore, be summarized that CO₂ injection resulting in solid volume increase and the incorporation of small carbonate reaction products into gel structures can improve the mechanical properties of the resultant cementitious system.

4. Conclusions

This study presented a comprehensive microstructural and chemo-mechanical phase characterization of CO₂-injected cement pastes at both early age (up to 1 day) and later age (7 and 28 days), providing new insights into the mechanisms underlying strength improvements observed in concrete with CO₂ mineralization. The key findings are summarized below.

- The CO₂ injection accelerated cement hydration, resulting in higher cumulative heat release and a 7% increase in 28-day compressive strength compared to control.
- Quantitative SEM and EDS analyses confirmed mineralization of CO₂, with carbonate volumes consistently 0.5-1.5% higher in CO₂-injected pastes and carbonate precipitates predominantly smaller than 5 μm.

- Early-age precipitation of C-S-H with reduced Ca/Si was observed, while the Ca/Si difference between control and CO₂ systems diminished at later age, indicating convergence of hydration pathways.
- Lower calcium concentration of the CO₂-injected paste's pore solution at early age further evidenced its consumption in the mineralization reaction. Nanoindentation results revealed that CaCO₃ crystals reinforced high-density C-S-H, leading to higher indentation modulus relative to control. The homogenized modulus values also demonstrated overall matrix densification.

In summary, these results demonstrate that CO_2 mineralization densifies the cement paste microstructure by filling nanoscale gel pores with fine calcium carbonate precipitates. This reinforces the C-S-H matrix and enhances mechanical performance. This mechanistic understanding directly supports and explains field-scale observations of improved compressive strength in CO_2 -injected concrete, thereby providing a critical scientific foundation for scaling CO_2 utilization technologies in the cement and concrete industry.

Acknowledgments

The authors gratefully acknowledge the Material Analysis and Research Laboratory (MARL) and Sid Pathak's Research Group at Iowa State University for performing SEM-EDS and nanoindentation, respectively, and Dalhousie University (Halifax, Nova Scotia) for performing the ICP-OES. Ryan Muir of CarbonCure Technologies is also acknowledged for helping with the paste sample preparation.

Declaration of Interest Statement

The authors report there are no competing interest to declare.

CRediT Author Statement

Yogiraj Sargam: Conceptualization, Methodology, Validation, Formal analysis, Data Curation, Writing- Original Draft, Writing- Review and Editing. Sean Monkman: Conceptualization, Methodology, Writing- Review and Editing, Supervision, Project administration. Vishnu Chaudhari: Formal analysis, Data curation, Writing- Review and Editing.

Funding

This research did not receive any specific grant from funding agencies in the public, commercial, or not-for-profit sectors.

References

- [1] Ostovari H, Sternberg A, Bardow A. Rock 'n' use of CO2: carbon footprint of carbon capture and utilization by mineralization. Sustainable Energy Fuels. 2020;4(9):4482–4496.
- [2] CO2 Sciences and the Global CO2 Initiative. Global Roadmap for Implementing CO2 Utilization [Internet]. 2016 [cited 2017 Feb 1]. Available from: https://www.globalco2initiative.org/documents/CO2U_ICEF_Roadmap_FIN AL 2016 12 07.pdf.
- [3] Monkman S. Sustainable Ready Mixed Concrete Production Using Waste CO2: A Case Study. SP-330 Proceedings Fourteenth International Conference: Recent Advances in Concrete Technology and Sustainability Issues. Beijing, China: American Concrete Institute; 2018. p. 163–174.
- [4] Berger RL, Young JF, Leung K. Acceleration of Hydration of Calcium Silicates by Carbon-Dioxide Treatment. Nature: Physical Science. 1972;240(97):16–18.
- [5] Monkman S, Hwang SD, Khayat K. Reduction in SCC form pressure through in-situ CO2 mineralization. Cement and Concrete Composites. 2024;152:105670.
- [6] Monkman S, Hwang SD, Khayat K. Rheology modification of flowable mortar with CO2. Cement and Concrete Composites. 2024;151:105584.
- [7] Monkman S, MacDonald M, Hooton RD, et al. Properties and durability of concrete produced using CO2 as an accelerating admixture. Cement and Concrete Composites. 2016;74:218–224.
- [8] Monkman S, Cialdella R, Pacheco J. Performance, Durability, and Life Cycle Impacts of Concrete Produced with CO2 as Admixture. ACI Materials Journal. 2023;120(1):53–62.
- [9] Monkman S, MacDonald M. On carbon dioxide utilization as a means to improve the sustainability of ready-mixed concrete. Journal of Cleaner Production. 2017;167:365–375.
- [10] Driver JG, Bernard E, Patrizio P, et al. Global decarbonization potential of CO₂ mineralization in concrete materials. Proc Natl Acad Sci USA. 2024;121(29):e2313475121.

- [11] Zajac M, Lechevallier A, Durdzinski P, et al. CO2 mineralisation of Portland cement: Towards understanding the mechanisms of enforced carbonation. Journal of CO2 Utilization. 2020;38:398–415.
- [12] Zajac M, Skibsted J, Durdzinski P, et al. Kinetics of enforced carbonation of cement paste. Cement and Concrete Research. 2020;131:106013.
- [13] Monkman S, Lee BEJ, Grandfield K, et al. The impacts of in-situ carbonate seeding on the early hydration of tricalcium silicate. Cement and Concrete Research. 2020;136:106179.
- [14] Monkman S, Sargam Y, Raki L. Comparing the effects of in-situ nano-calcite development and ex-situ nano-calcite addition on cement hydration. Construction and Building Materials. 2022;321:126369.
- [15] Stefaniuk D, Hajduczek M, Weaver JC, et al. Cementing CO2 into C-S-H: A step toward concrete carbon neutrality. Xu Y-J, editor. PNAS Nexus. 2023;2(3):pgad052.
- [16] ASTM C150. Specification for Portland Cement [Internet]. ASTM International; 2005 [cited 2022 Feb 1]. Available from: http://www.astm.org/cgi-bin/resolver.cgi?C150-05.
- [17] Monkman S, Sargam Y, Naboka O, et al. Early age impacts of CO2 activation on the tricalcium silicate and cement systems. Journal of CO2 Utilization. 2022;65:102254.
- [18] ASTM C192. Practice for Making and Curing Concrete Test Specimens in the Laboratory [Internet]. ASTM International; 2015 [cited 2022 Feb 2]. Available from: http://www.astm.org/cgi-bin/resolver.cgi?C192C192M-15.
- [19] ASTM C109 / C109M-16a. Test Method for Compressive Strength of Hydraulic Cement Mortars (Using 2-in. or [50-mm] Cube Specimens) [Internet]. West Conshohocken, PA: ASTM International; 2016 [cited 2020 Mar 16]. Available from: http://www.astm.org/cgi-bin/resolver.cgi?C109C109M-16A.
- [20] Duchesne J, Bérubé MA. Evaluation of the validity of the pore solution expression method from hardened cement pastes and mortars. Cement and Concrete Research. 1994;24(3):456–462.
- [21] Sargam Y, Wang K. Quantifying dispersion of nanosilica in hardened cement matrix using a novel SEM-EDS and image analysis-based methodology. Cement and Concrete Research. 2021;147:106524.

- [22] Chen JJ, Sorelli L, Vandamme M, et al. A Coupled Nanoindentation/SEM-EDS Study on Low Water/Cement Ratio Portland Cement Paste: Evidence for C-S-H/Ca(OH) 2 Nanocomposites. Journal of the American Ceramic Society [Internet]. 2010 [cited 2022 Feb 4]; doi: 10.1111/j.1551-2916.2009.03599.x.
- [23] Long W-J, Gu Y, Xiao B-X, et al. Micro-mechanical properties and multi-scaled pore structure of graphene oxide cement paste: Synergistic application of nanoindentation, X-ray computed tomography, and SEM-EDS analysis. Construction and Building Materials. 2018;179:661–674.
- [24] Wilson W, Sorelli L, Tagnit-Hamou A. Automated coupling of NanoIndentation and Quantitative Energy-Dispersive Spectroscopy (NI-QEDS): A comprehensive method to disclose the micro-chemo-mechanical properties of cement pastes. Cement and Concrete Research. 2018;103:49–65.
- [25] Oliver WC, Pharr GM. An improved technique for determining hardness and elastic modulus using load and displacement sensing indentation experiments. J Mater Res. 1992;7(6):1564–1583.
- [26] Mori T, Tanaka K. Average stress in matrix and average elastic energy of materials with misfitting inclusions. Acta Metallurgica. 1973;21(5):571–574.
- [27] Brown L, Allison PG, Sanchez F. Use of nanoindentation phase characterization and homogenization to estimate the elastic modulus of heterogeneously decalcified cement pastes. Materials & Design. 2018;142:308–318.
- [28] da Silva WRL, Němeček J, Štemberk P. Application of multiscale elastic homogenization based on nanoindentation for high performance concrete. Advances in Engineering Software. 2013;62–63:109–118.
- [29] Sebastiani M, Moscatelli R, Ridi F, et al. High-resolution high-speed nanoindentation mapping of cement pastes: Unravelling the effect of microstructure on the mechanical properties of hydrated phases. Materials & Design. 2016;97:372–380.
- [30] Jennings HM. A model for the microstructure of calcium silicate hydrate in cement paste. Cement and Concrete Research. 2000;30(1):101–116.
- [31] Scrivener KL, Nonat A. Hydration of cementitious materials, present and future. Cement and Concrete Research. 2011;41(7):651–665.

- [32] Kurihara R, Maruyama I. Revisiting Tennis-Jennings method to quantify low-density/high-density calcium silicate hydrates in Portland cement pastes. Cement and Concrete Research. 2022;156:106786.
- [33] Bazzoni A. Study of early hydration mechanisms of cement by means of electron microscopy. 2014 [cited 2022 Feb 16]; doi: 10.5075/EPFL-THESIS-6296.
- [34] Gallucci E, Mathur P, Scrivener K. Microstructural development of early age hydration shells around cement grains. Cement and Concrete Research. 2010;40(1):4–13.
- [35] Briki Y, Zajac M, Haha MB, et al. Impact of limestone fineness on cement hydration at early age. Cement and Concrete Research. 2021;147:106515.
- [36] Sargam Y, Wang K, Tsyrenova A, et al. Effects of anionic and nonionic surfactants on the dispersion and stability of nanoSiO2 in aqueous and cement pore solutions. Cement and Concrete Research. 2021;144:106417.
- [37] Monkman S. On the mechanism of using carbon dioxide as a beneficial concrete admixture. Beijing, China; 2018.
- [38] Richardson IG. The nature of C-S-H in hardened cements. Cement and Concrete Research. 1999;29(8):1131–1147.
- [39] Richardson IG. Tobermorite/jennite- and tobermorite/calcium hydroxide-based models for the structure of C-S-H: applicability to hardened pastes of tricalcium silicate, β-dicalcium silicate, Portland cement, and blends of Portland cement with blast-furnace slag, metakaolin, or silica fume. Cement and Concrete Research. 2004;34(9):1733–1777.
- [40] Li X, Scrivener KL. Impact of ZnO on C3S hydration and C-S-H morphology at early ages. Cement and Concrete Research. 2022;154:106734.
- [41] Lothenbach B, Le Saout G, Gallucci E, et al. Influence of limestone on the hydration of Portland cements. Cement and Concrete Research. 2008;38(6):848–860.
- [42] Yan Y, Yang S-Y, Miron GD, et al. Effect of alkali hydroxide on calcium silicate hydrate (C-S-H). Cement and Concrete Research. 2022;151:106636.
- [43] Vollpracht A, Lothenbach B, Snellings R, et al. The pore solution of blended cements: a review. Mater Struct. 2016;49(8):3341–3367.

- [44] da Silva WRL, Němeček J, Štemberk P. Methodology for nanoindentation-assisted prediction of macroscale elastic properties of high performance cementitious composites. Cement and Concrete Composites. 2014;45:57–68.
- [45] Němeček J, Králík V, Šmilauer V, et al. Tensile strength of hydrated cement paste phases assessed by micro-bending tests and nanoindentation. Cement and Concrete Composites. 2016;73:164–173.
- [46] Hughes JJ, Trtik P. Micro-mechanical properties of cement paste measured by depth-sensing nanoindentation: a preliminary correlation of physical properties with phase type. Materials Characterization. 2004;53(2–4):223–231.
- [47] Constantinides G, Ulm F-J, Van Vliet K. On the use of nanoindentation for cementitious materials. Mat Struct. 2003;36(3):191–196.
- [48] Constantinides G, Ulm F-J. The nanogranular nature of C–S–H. Journal of the Mechanics and Physics of Solids. 2007;55(1):64–90.
- [49] Constantinides G, Ulm F-J. The effect of two types of C-S-H on the elasticity of cement-based materials: Results from nanoindentation and micromechanical modeling. Cement and Concrete Research. 2004;34(1):67–80.
- [50] Wei Y, Gao X, Liang S. A combined SPM/NI/EDS method to quantify properties of inner and outer C-S-H in OPC and slag-blended cement pastes. Cement and Concrete Composites. 2018;85:56–66.
- [51] Pelisser F, Gleize PJP, Mikowski A. Effect of the Ca/Si Molar Ratio on the Micro/nanomechanical Properties of Synthetic C-S-H Measured by Nanoindentation. J Phys Chem C. 2012;116(32):17219–17227.
- [52] Manzano H, Dolado JS, Ayuela A. Elastic properties of the main species present in Portland cement pastes. Acta Materialia. 2009;57(5):1666–1674.
- [53] Allen AJ, Thomas JJ, Jennings HM. Composition and density of nanoscale calcium–silicate–hydrate in cement. Nature Materials. 2007;6(4):311–316.
- [54] Thomas JJ, Jennings HM, Allen AJ. Relationships between Composition and Density of Tobermorite, Jennite, and Nanoscale CaO-SiO2 -H2O. The Journal of Physical Chemistry C. 2010;114(17):7594–7601.
- [55] Sargam Y, Wang K. Influence of dispersants and dispersion on properties of nanosilica modified cement-based materials. Cement and Concrete Composites. 2021;118:103969.

Tables

Table 1. Chemical analyses of the cement used in the study (phases reported are weight percent, potential phase composition via calculation); LOI: Loss on Ignition; C_3S : Tricalcium Silicate; C_2S : Dicalcium Silicate; C_3A : Tricalcium Aluminate; C_4AF : Tetra Calcium Aluminoferrite

	CaO	SiO ₂	Al ₂ O ₃	SO₃	Fe ₂ O ₃	MgO	LOI	C ₃ S	C ₂ S	C ₃ A	C₄AF
Amount	64.0	20.1	4.9	3.0	3.3	0.9	2.8	62.0	11.0	7.0	10.0

Table 2. Quantitative calorimetry curve analysis

Metric	Control	CO ₂
Thermal indicator of set (h)	3.12	3.26
Acceleration slope (mW·g ⁻¹ ·h ⁻¹)	0.49	0.71
Time at peak power (h)	7.49	6.51
Heat flow at peak (mW/g _{cement})	2.84	3.30
Total heat at 24 hours (J/g _{cement})	149.9	160.8
Relative total heat at 24 hours	100%	107%

Table 3. Input parameters from nanoindentation data and estimated homogenized moduli using the Mori-Tanaka method

Paste system	Age of paste (days)	Indentation modulus of reinforced HD CSH/calcium carbonate (GPa)	Porosity determined from SEM (%)	Estimated homogenized modulus of paste (GPa)	
	1	13.9 ± 0.4	8.9	21.6 ± 0.6	
Control	7	14.6 ± 0.6	7.2	23.1 ± 0.4	
	28	21.7 ± 0.5	6.5	31.7 ± 0.3	
	1	15.6 ± 1.4	9.9	22.9 ± 1.0	
CO_2	7	21.8 ± 1.4	6.8	31.9 ± 0.6	
	28	22.3 ± 0.4	7.0	30.6 ± 0.2	

Figures

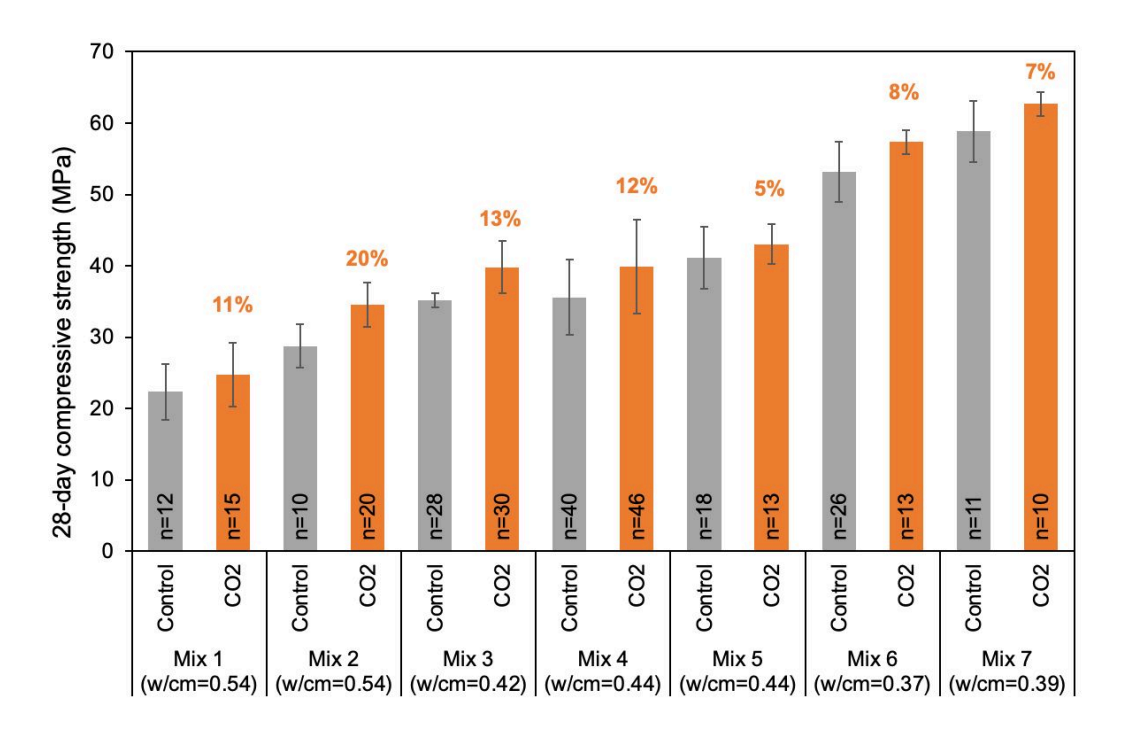


Fig. 1. Example of compressive strength improvement in industrially produced concrete when CO₂ is used as an admixture. The number of samples tested for strength are denoted as 'n', error bars represent the standard deviation, and percentage strength improvements are shown above the CO₂ bars

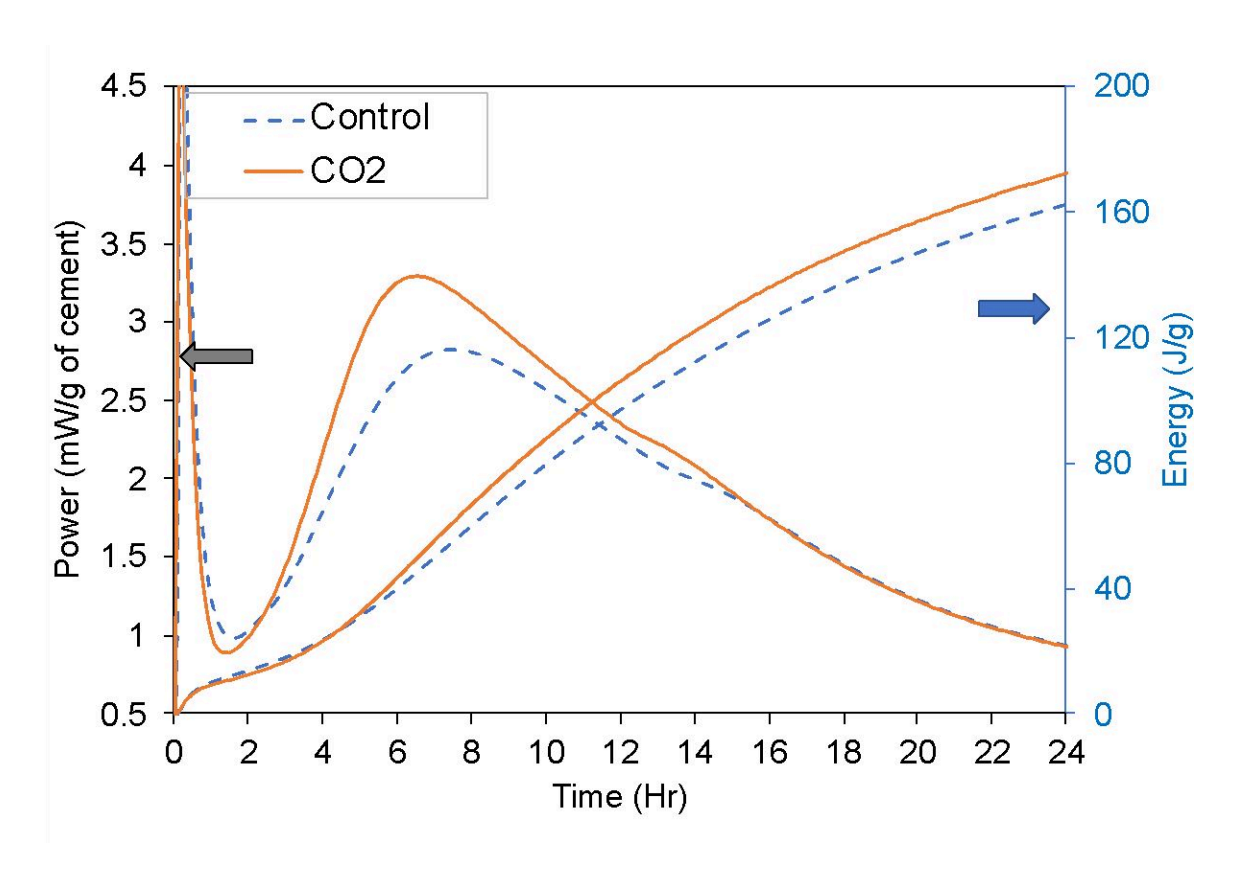


Fig. 2. Effect of CO₂ injection on heat of hydration and cumulative energy release (arrows indicate the primary and secondary y-axes)

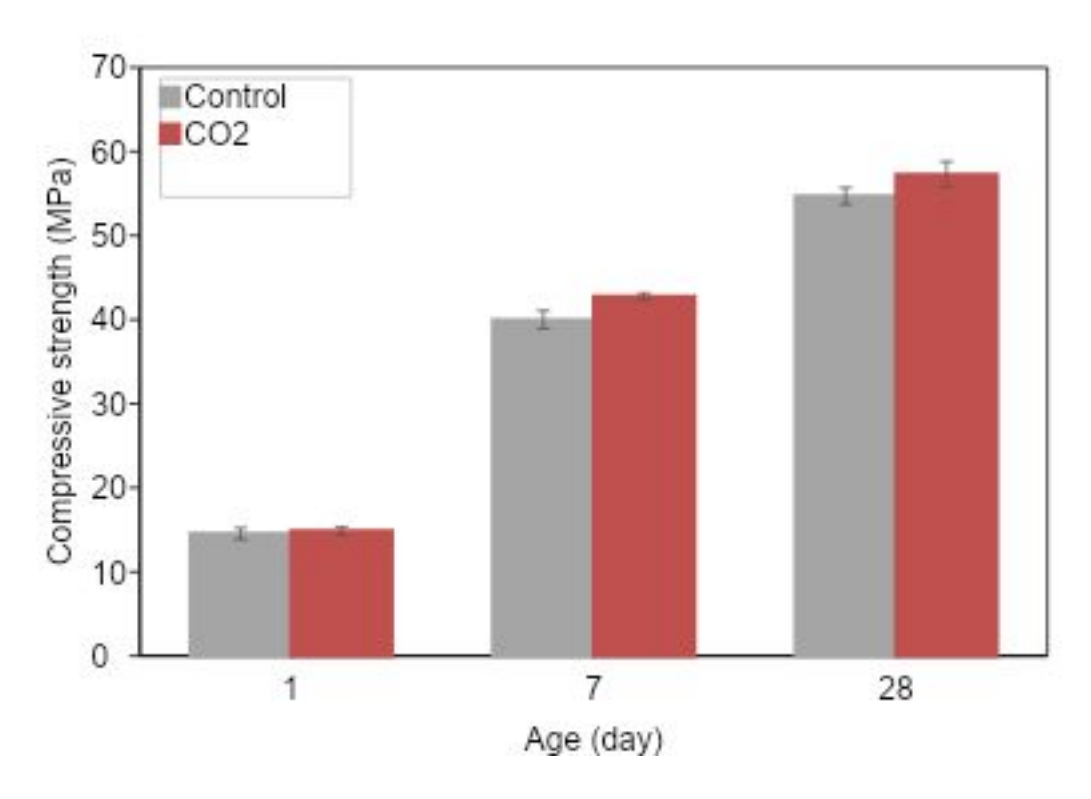


Fig. 3. Effect of CO₂ injection on compressive strength of cement paste

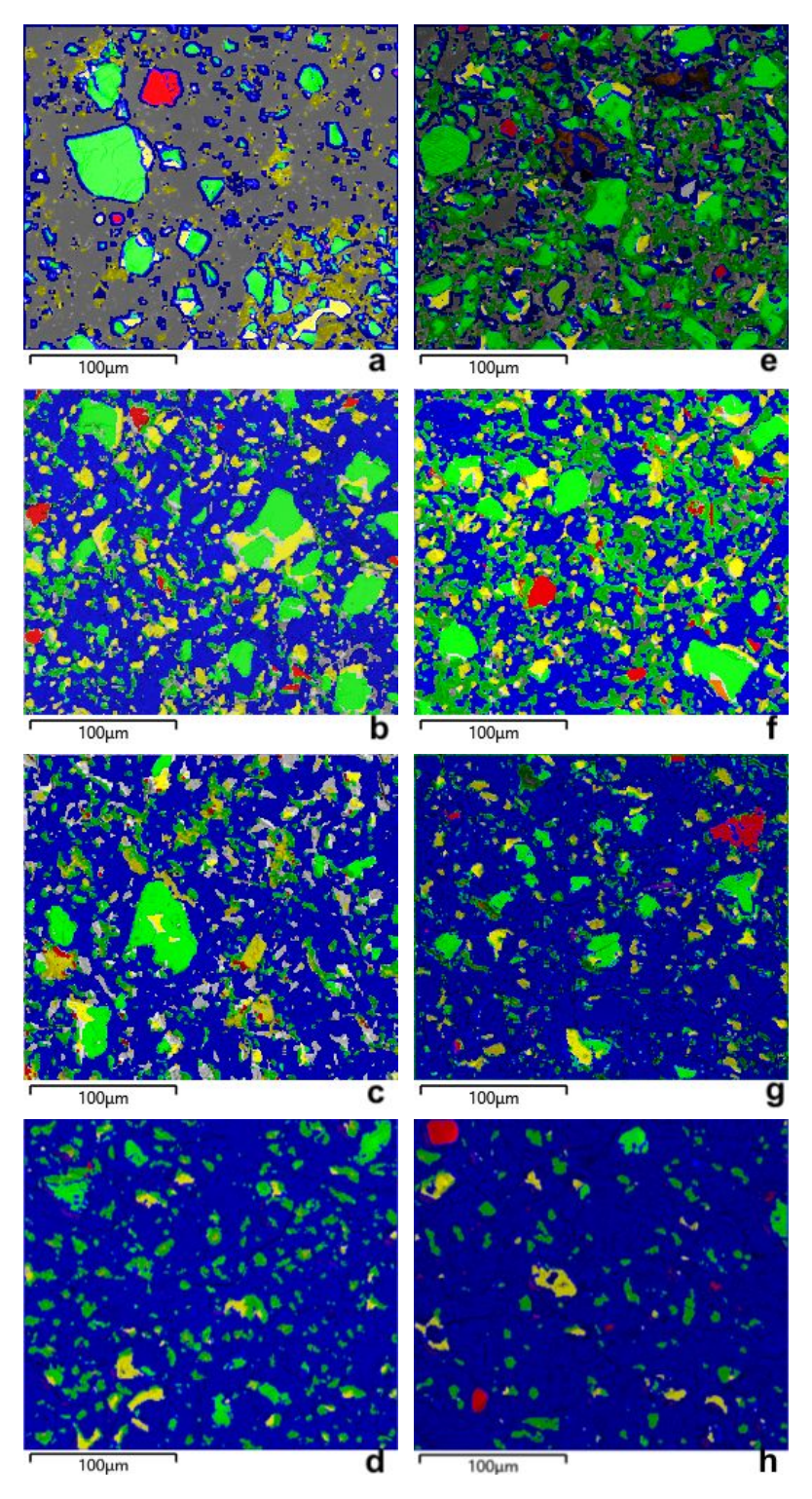


Fig. 4. Phase segmentation of BSE micrographs (based on EDS) with false colors attributed to phases: Green- C_3S/C_2S , Yellow- C_3A/C_4AF , Purple- AFt/AFm, Blue- C-S-H/CH, Red: limestone present in cement, Orange: carbonates formed

through CO_2 mineralization (see **Fig. 5** for an example of a masked image); (a-d) and (e-h) shows micrographs of control and CO_2 samples, respectively, at ages of 5 minute, 1 day, 7 days, and 28 day

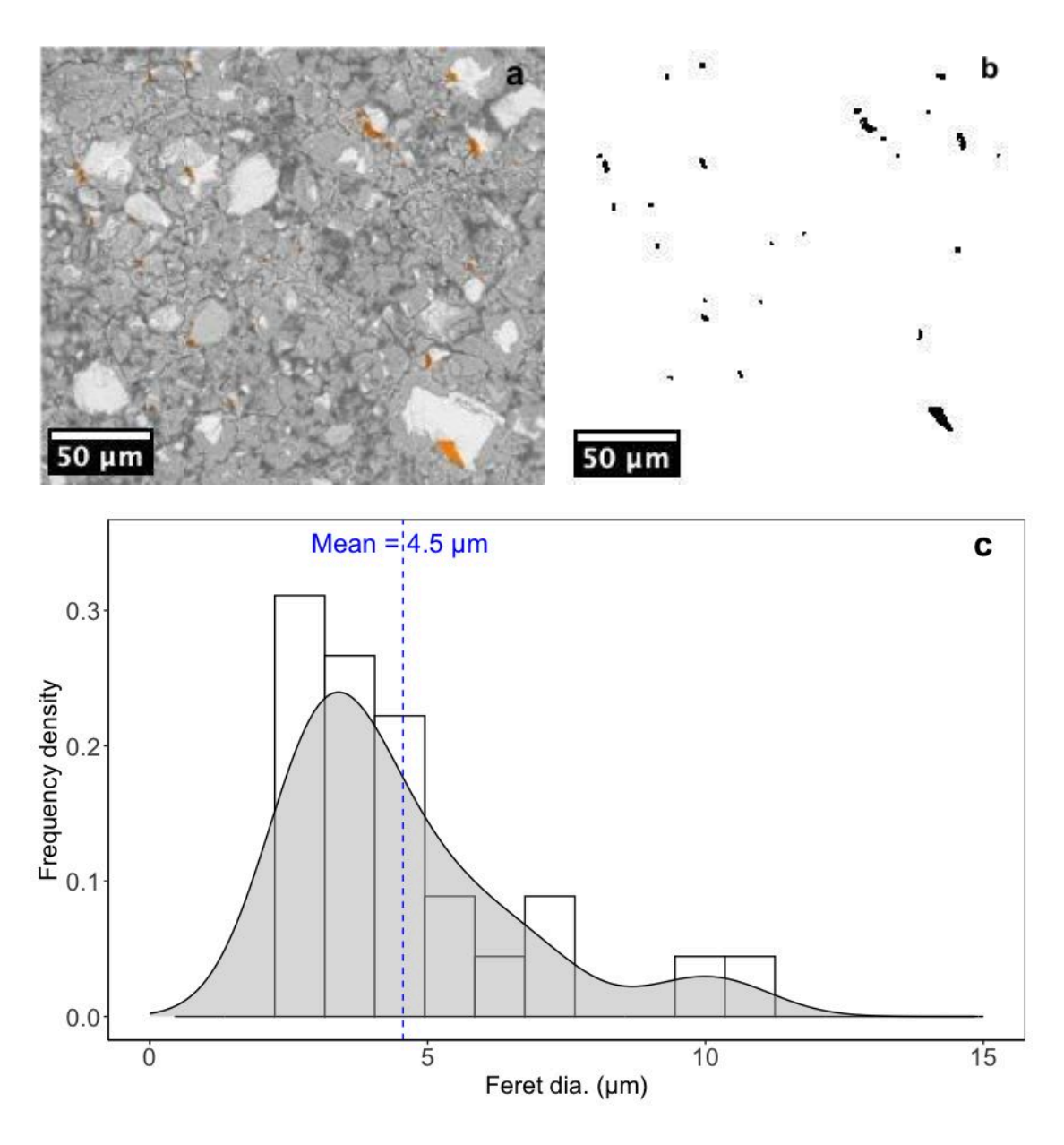


Fig. 5. (a) BSE micrograph and (b) Binary image showing carbonates formed (orange-colored) through CO₂ mineralization; (c) Size (Feret diameter) distribution of mineralized carbonate products

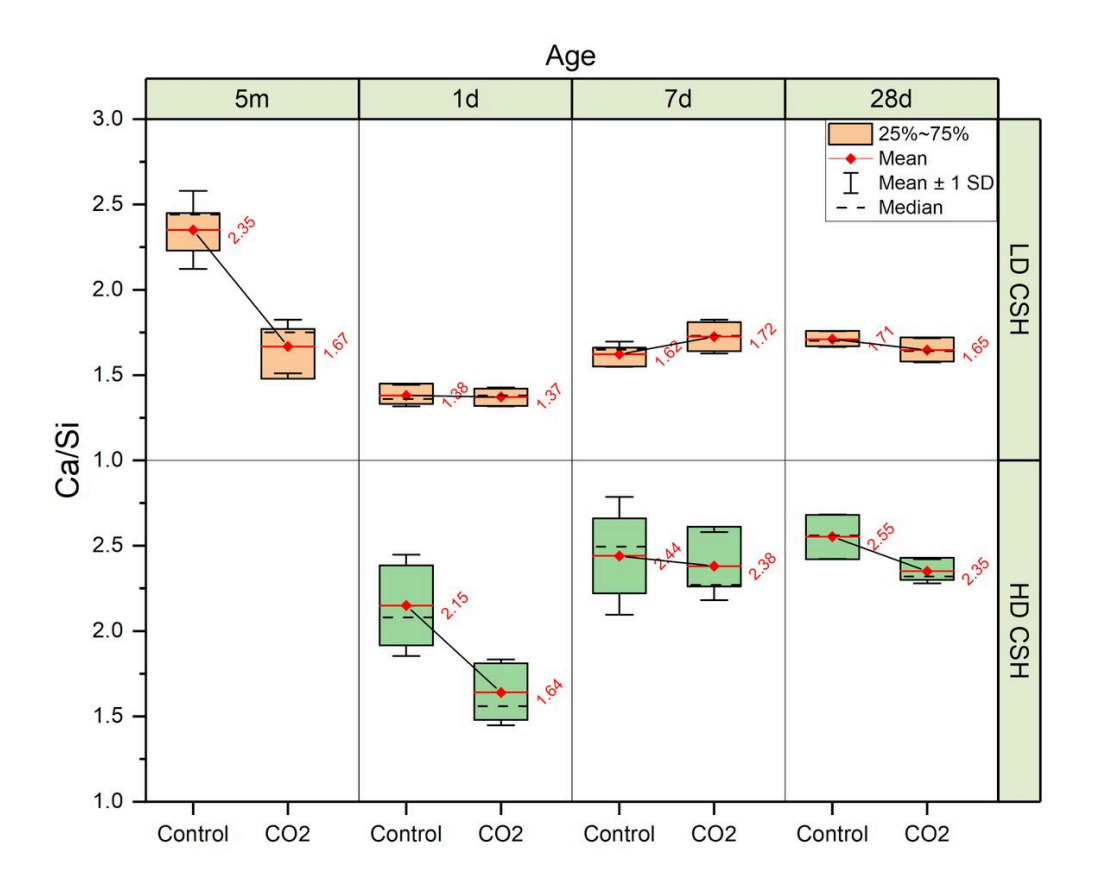


Fig. 6. Ca/Si ratio of LD and HD C-S-H determined from SEM-EDS analysis

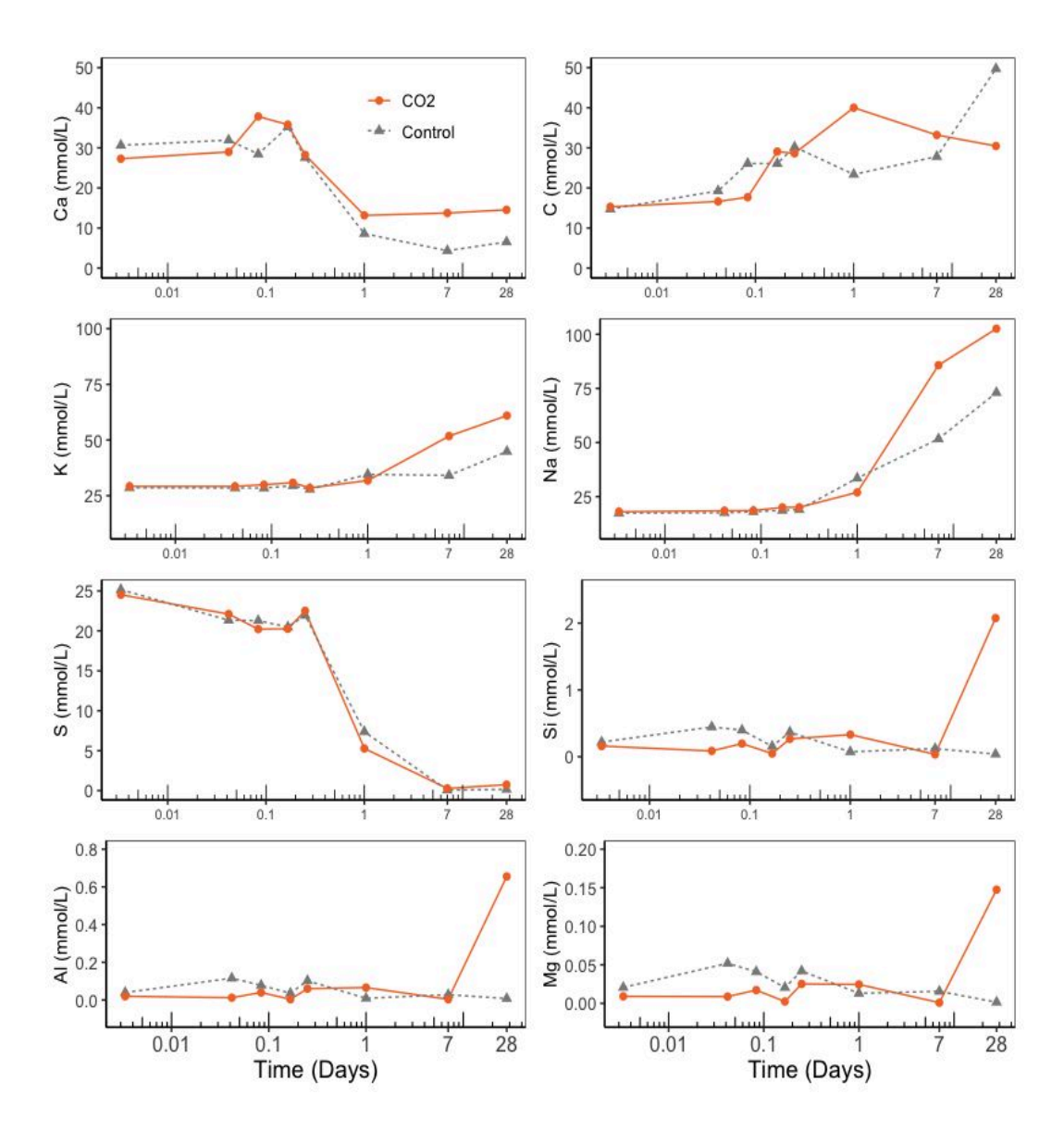


Fig. 7. Measured elemental concentrations of cement pore solutions

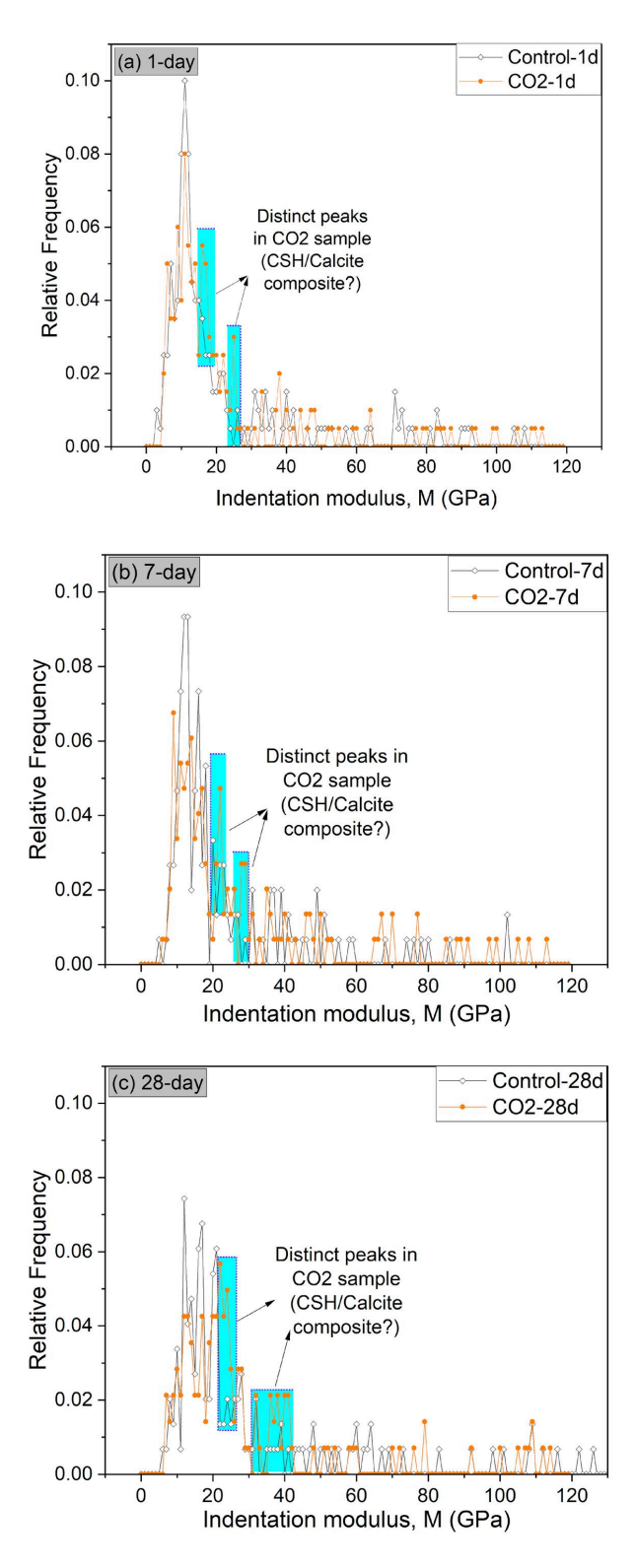


Fig. 8. Frequency distributions of indentation modulus at (a) 1 day; (b) 7 day; and (c) 28 day

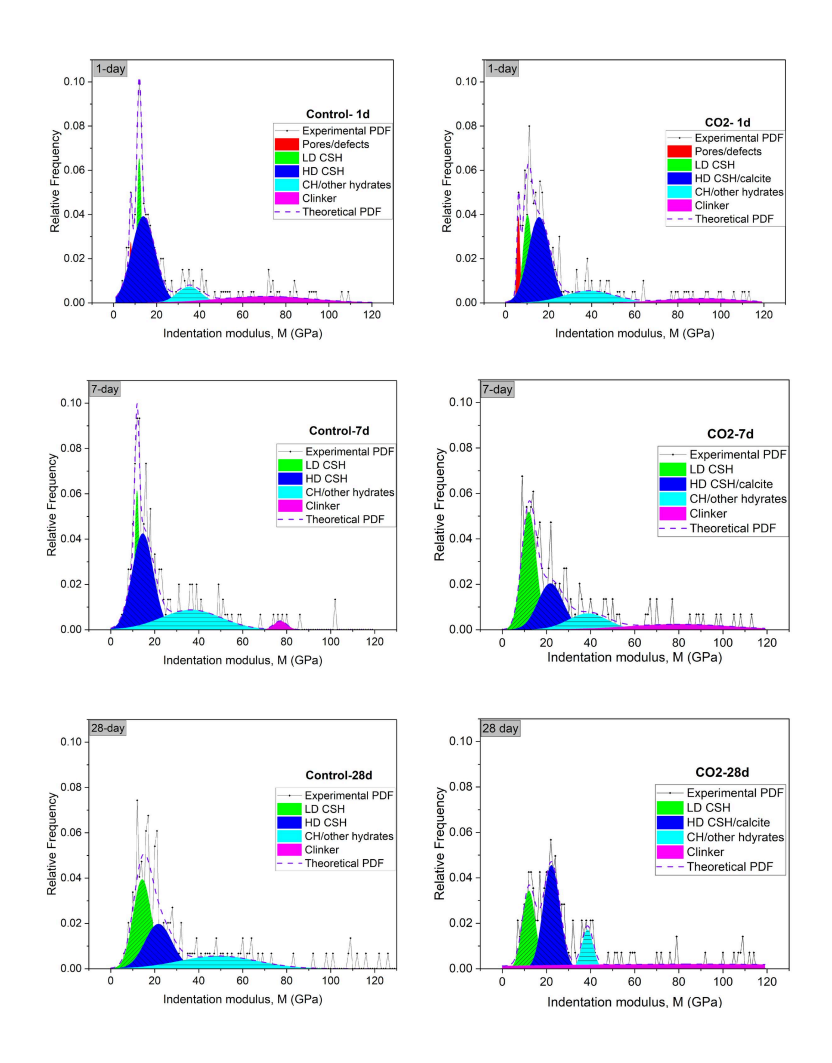
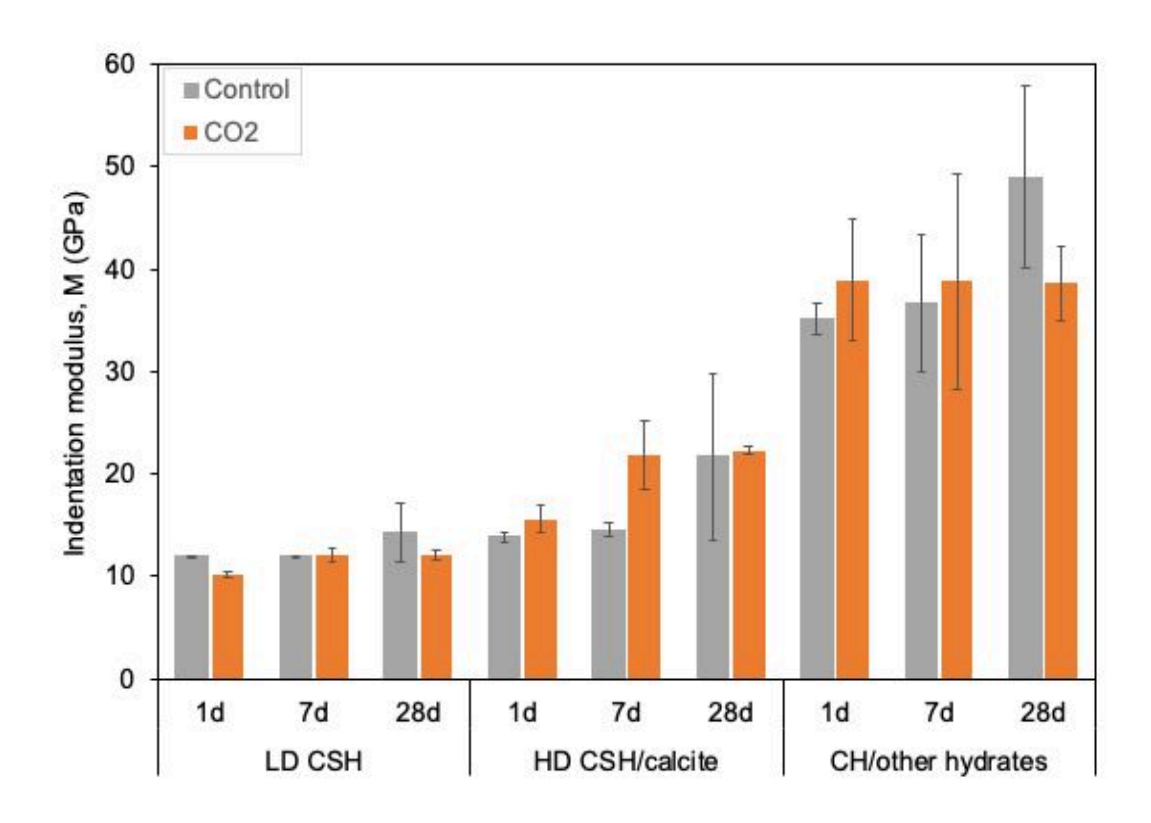


Fig. 9. Experimental and best-fit theoretical probability density functions for indentation modulus (deconvoluted peaks are shown in color, representing phases in ascending order of modulus from left to right)



Supplementary information

for

CO₂-injected Cement Paste: Insights into Microstructural and Chemo-mechanical Changes

Yogiraj Sargam⁴, Sean Monkman⁵, Vishnu Chaudhari⁶

Industrial Data

Table S1 shows the mix design, fresh, and hardened properties of concrete mixes obtained from different ready-mix concrete producers in North America. Statistically significant number of cylindrical samples (4-inch × 8-inch) were tested for compressive strength after 28 days of curing. CO₂ was used as an admixture in these mixes at 0.1 to 0.2% by weight of cement, and it improved the compressive strength by 5 to 20% without significant impacts on the fresh air content or workability.

⁴ **Corresponding author**; <u>yogirajsargam@gmail.com</u>; CarbonCure Technologies, 161 Joseph Zatzman Drive, Dartmouth B3B 1M7, Canada

⁵ <u>sean.monkman@gmail.com</u>; Six Down Consulting, Austin, Texas, USA

⁶ vchaudhari@carboncure.com; CarbonCure Technologies, 161 Joseph Zatzman Drive, Dartmouth B3B 1M7, Canada

Table S1. Design and properties of concrete mixes with CO₂ as an admixture (w/cm: water-to-cementitious ratio; bwc: by weight of cement; COV: coefficient of variation)

Detail	Constituent/Property	Unit	Mix 1		Mix 2		Mix 3		Mix 4		Mix 5		Mix 6		Mix 7	
			Control	CO2												
Concrete mix design	w/cm	Ratio	0.54	0.54	0.54	0.54	0.42	0.42	0.44	0.44	0.44	0.44	0.37	0.37	0.39	0.39
	Cementitious	kg/m³	297	297	280	280	307	310	335	335	335	335	454	454	415	415
	Water	kg/m³	161	161	150	150	128	131	148	148	148	148	168	168	163	163
	Coarse aggregate	kg/m³	994	994	867	867	909	909	997	997	1083	1083	981	981	1061	1061
	Fine aggregate	kg/m³	858	858	965	965	871	860	834	834	789	789	682	682	878	878
	Water reducer	% bwc	0.3	0.3	0.1	0.1	0.5	0.5	0.2	0.2	0.25	0.25	0.1	0.1	0.1	0.1
	CO ₂	% bwc	-	0.1	-	0.1	-	0.2	-	0.1	-	0.2	-	0.15	-	0.2
Fresh properties	Avg. slump	mm	119	132	129	94	135	124	118	102	141	140	138	160	177	182
	Avg. air	%	3.0	3.1	6.7	6.5	6.8	7.6	6.0	6.3	3.9	4.2	2.3	2.1	-	-
Hardened properties	28d comp. strength	MPa	22.34	24.75	28.76	34.50	35.15	39.80	35.59	39.92	41.16	43.04	53.16	57.34	58.82	62.66
	Stdev	MPa	3.90	4.50	3.05	3.11	1.03	3.62	5.26	6.57	4.33	2.80	4.21	1.67	4.23	1.68
	cov	%	17%	18%	11%	9%	3%	9%	15%	16%	11%	7%	8%	3%	7%	3%
	Strength vs control	%	100%	111%	100%	120%	100%	113%	100%	112%	100%	105%	100%	108%	100%	107%
	Samples	#	12	15	10	20	28	30	40	46	18	13	26	13	11	10

SEM microanalysis

The micrographs obtained from SEM analysis at magnifications of 150×, 500×, and 1500× are shown in Figs. S1-S4. The analyzed area is also highlighted in rectangular shape. The EDS mapping of all 500× micrographs were performed an example of which is shown in Fig. S5 (7-day aged control sample).

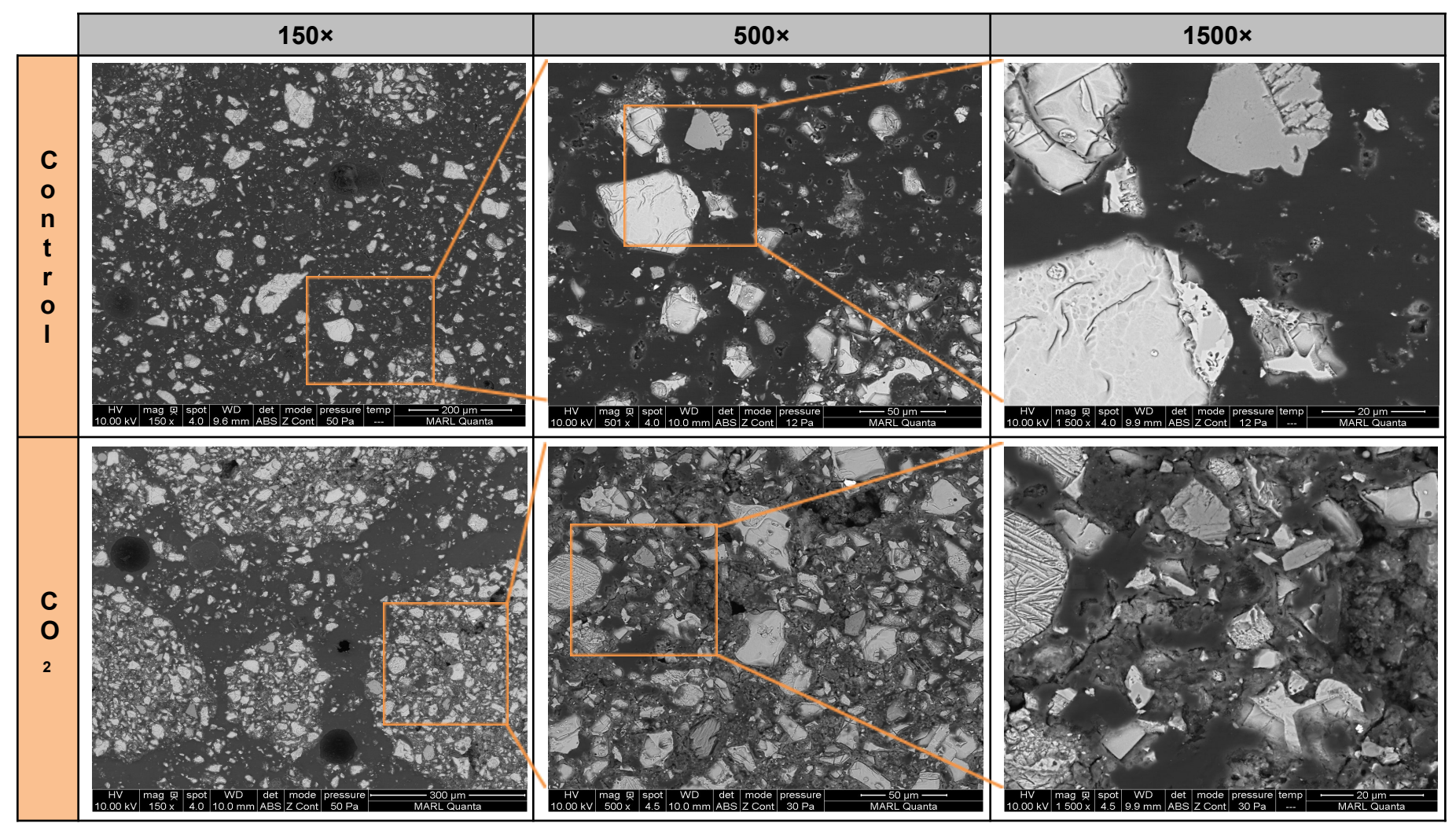


Fig. S1. BSE micrographs of cement paste samples aged 5 minute

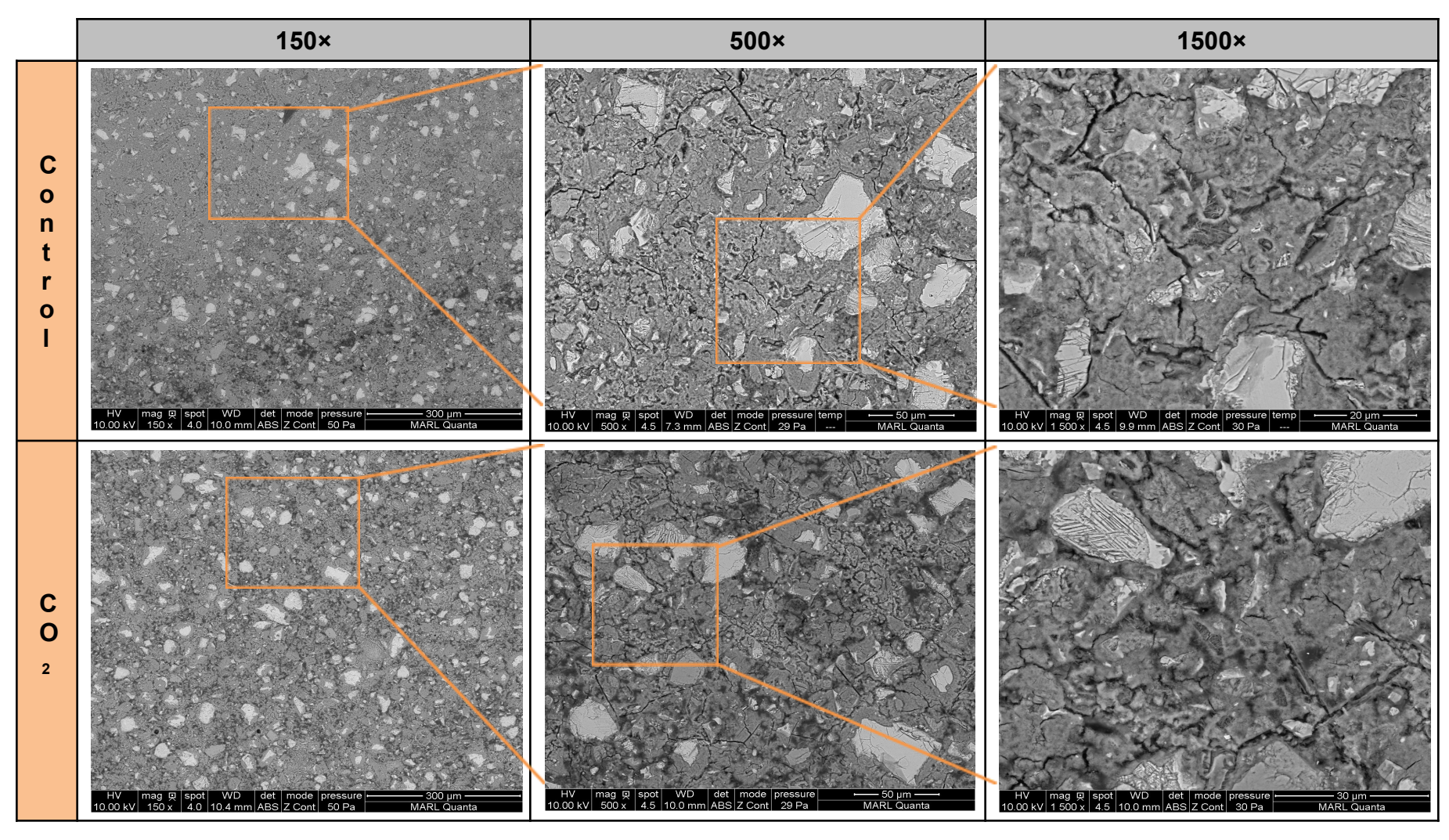


Fig. S2. BSE micrographs of cement paste samples aged 1 day

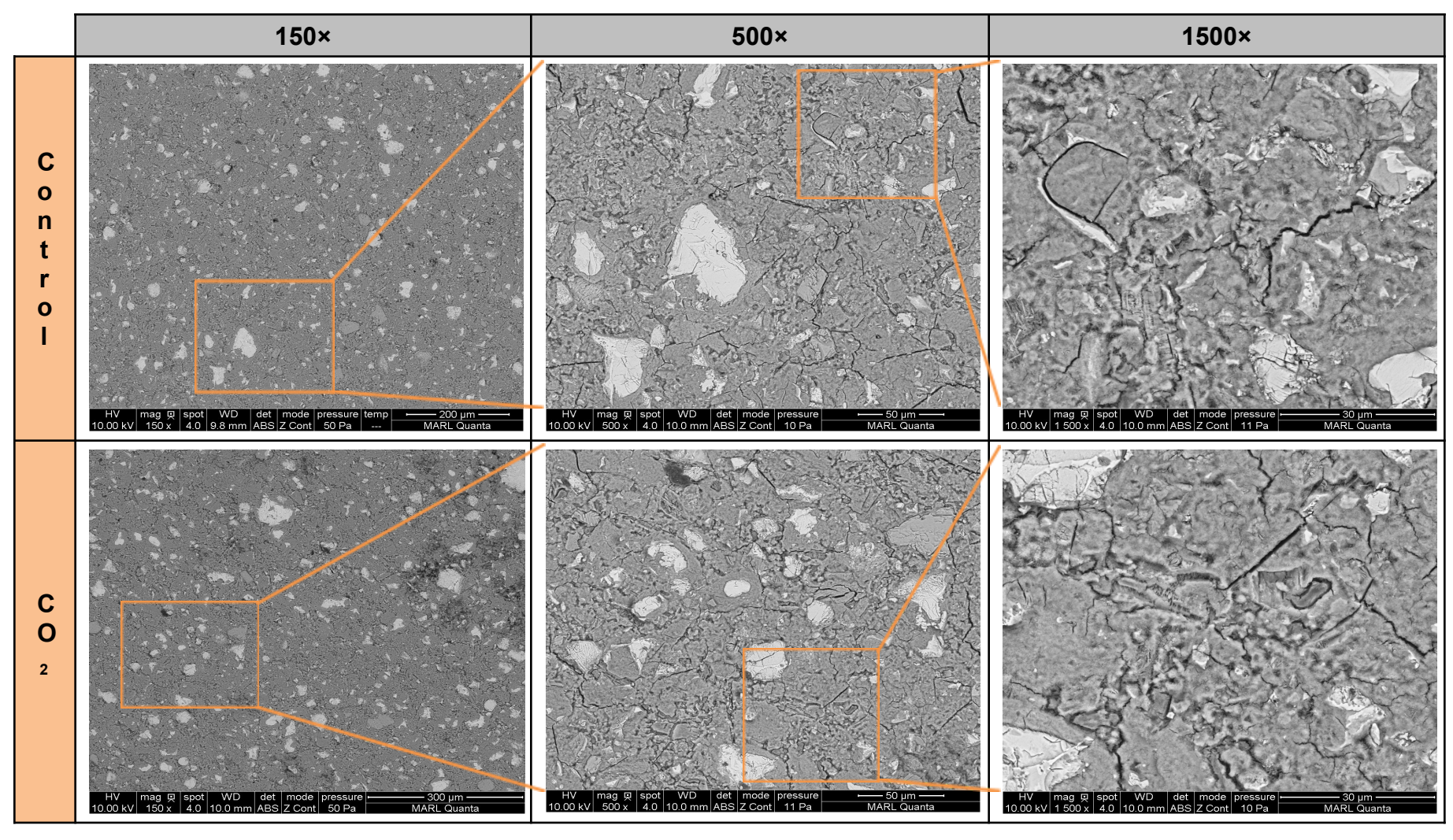


Fig. S3. BSE micrographs of cement paste samples aged 7 day

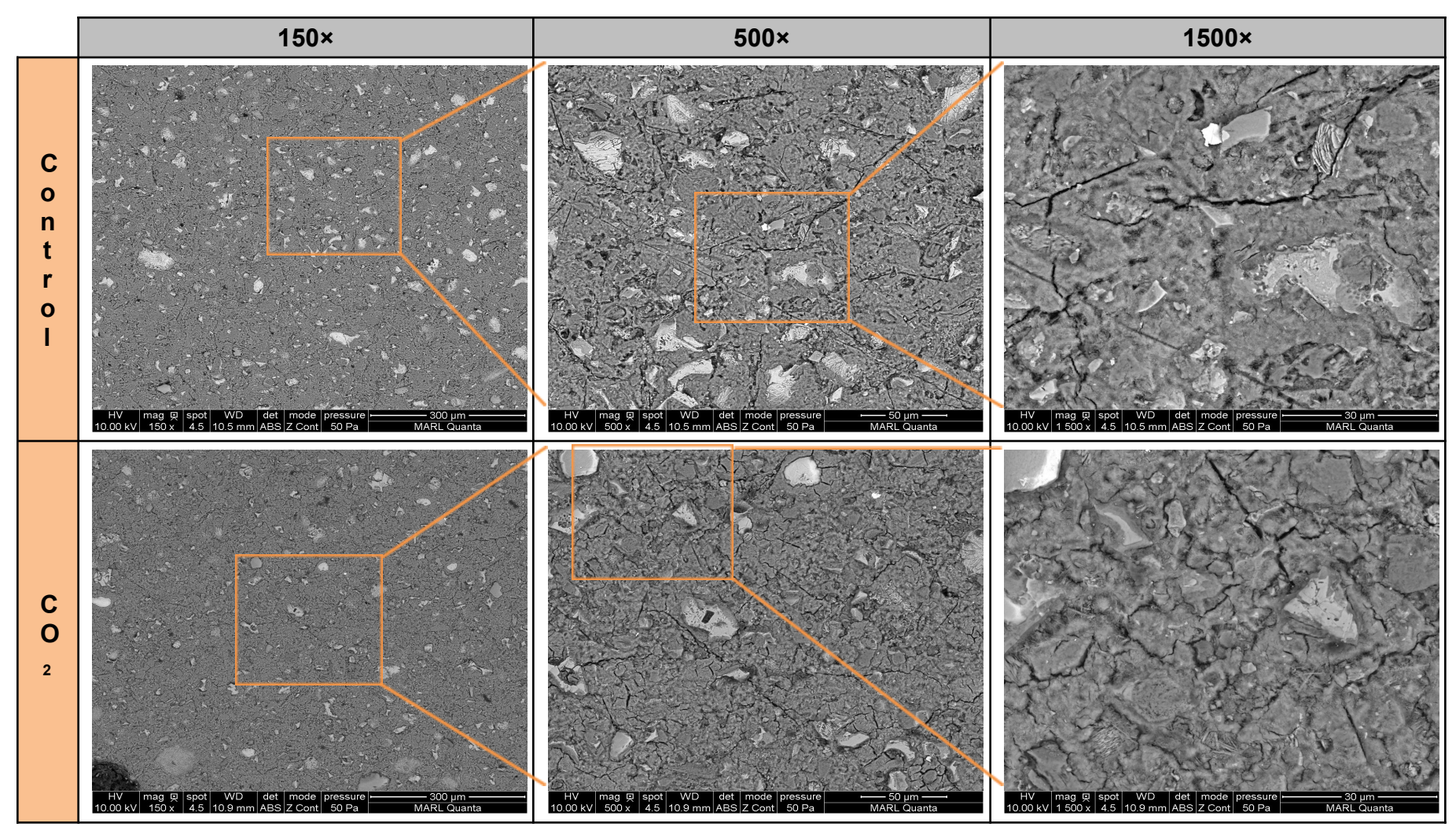


Fig. S4. BSE micrographs of cement paste samples aged 28 day

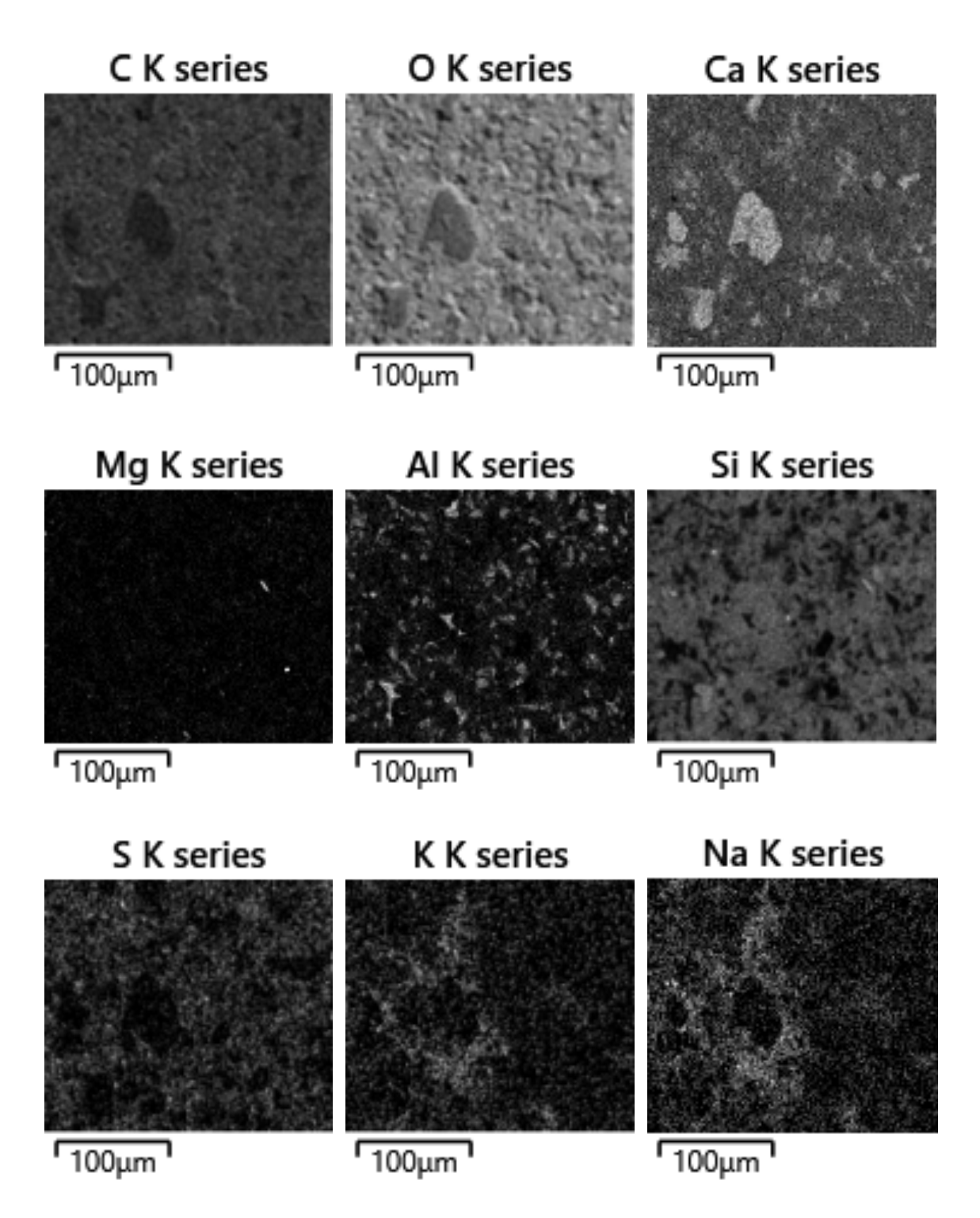


Fig. S5. Example showing EDS mapping of 7-day aged control sample at 500X magnification (corresponding BSE micrograph shown in **Fig. S3**)

3. Nanoindentation

The experimental indentation modulus data obtained from nanoindentation was deconvolution using the curve-fitting function in *Originlab* [1]. Gaussian fitting function was employed for this purpose. The individual peaks were deconvoluted so as to obtain a cumulative fitted curve with the coefficient of determination (R^2) greater than 0.9. The experimental data and the fitted curves corresponding to the control and CO_2 -activated samples at 1, 7, and 28 day are presented in Fig. S6.

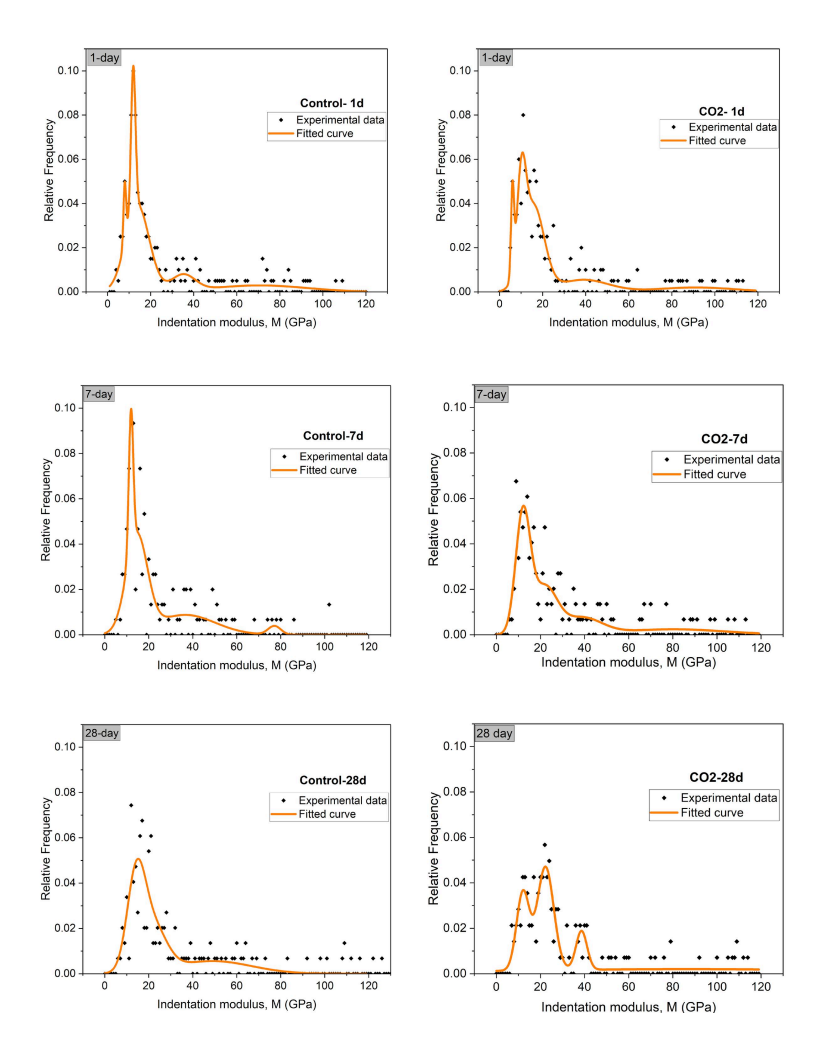


Fig. S6. The cumulative Gaussian curve fitted to the experimental frequency distribution of indentation modulus

References

[1] Origin (Pro), (n.d.). https://www.originlab.com.